

Master of science thesis

**Initial steps toward MRI-based treatment planning for
external radiotherapy**

Sara Thörnqvist

Supervisors: Sara Brockstedt, Crister Ceberg, Tommy Knöös

Department of Medical Physics
Lund University

Table of contents

Abstract	1
1. Introduction	2
1.1 The aim.....	2
2. Background	3
2.1 MRI	3
2.2 Image distortions.....	3
2.2.1 Object-induced distortion.....	4
2.2.2 System-induced distortion.....	4
2.2.3 Phantom used to evaluate geometric distortions	5
2.3 UTE pulse sequences.....	5
2.4 External radiotherapy	76
2.4.1 Treatment delivery techniques	7
2.4.2 CT-based treatment planning	7
2.4.3 MRI-based treatment planning.....	8
3. Methods	9
3.1 Evaluation of distortion	9
3.1.1 Phantom used for the measurements	9
3.1.2 Image acquisition	9
3.2 The UTE pulse sequence.....	10
3.3 Image post processing	11
3.3.1 Matching of the images for evaluation of distortion	11
3.3.2 Segmentation.....	11
3.4 External radiotherapy treatment planning.....	12
4. Results	13
4.1 Image distortions.....	13
4.2 The UTE pulse sequence.....	16
4.3 Segmentation of bone and air in the head.....	18
4.3 Treatment planning with bulk densities.....	19
4.3.1 3D CRT.....	19
4.3.2 IMRT	23
5. Discussion	27
5.1 Distortion	27
5.2 The UTE pulse sequence.....	29
5.3 Segmentation	30
5.4 Treatment planning	31
5.4.1 3D CRT.....	31
5.4.2 IMRT	32
5.5 Future work.....	33
6. Conclusion	34
Acknowledgements	35
References	36
7. Appendix	38

Abstract

Introduction; The aim of this study was to examine the possibilities for MRI-based radiotherapy treatment planning. The work included evaluation of geometric image distortions in MR-images, investigations of how segmentation of bone could be performed from images acquired with the ultra short time of echo (UTE) pulse sequence and assessment of dosimetric differences between treatment planning based on these images as compared to the original CT-based treatment plans.

Methods: A phantom with a well-defined rod geometry was used for the studying of geometric distortions in the imaging plane in MR-images. The ability of the UTE pulse sequence to visualize bone and other tissues with short T2-relaxation, was investigated by imaging the head of four healthy volunteers and bone, air and soft tissues were segmented from these images. The dosimetric accuracy expected from such segmented images, as well as from images where the head was treated as one homogenous volume, was compared to the gold standard of using CT-images. The dosimetric evaluation involved nine patients with existing conformal treatment plans and three patients with existing intensity modulated treatment plans.

Results: The geometric distortions in the imaging plane were in most cases less than the 2 mm demand in radiotherapy within the investigated volume and with the vendor's distortion correction applied. Segmentation was feasible using the UTE pulse sequence although some areas were misclassified. For conformal radiotherapy, dose calculations based on the segmented images showed a very close resemblance to the original CT-based plans in regard to dose volume histogram (DVH), dose to planning target volume (PTV) and dose to organ at risk (OAR) although approximating the head as one homogenous volume gave clinically acceptable deviations as well. This trend was also seen for the intensity modulated radiotherapy (IMRT) plans with the same optimization as in the original treatment plan however, making a new optimization based on the derived plans resulted in large deviations in DVH and dose to OAR, possibly a result from misclassifications in the segmentation.

Conclusion: Adding the UTE pulse sequence to the T1W- and the T2W-pulse sequences used when imaging patients obviously result in a prolonged scan time (of about 10 min) but has the advantage of making a more accurate treatment planning possible and could lead to MRI being used even in more complicated cases however, more patients are needed for evaluation. To completely fulfill the aim of this study, scanning a patient with both modalities is necessary since it could reveal the performance of the segmentation method and enable a dosimetric evaluation of the MRI-images to be conducted.

1. Introduction

In oncology, magnetic resonance imaging (MRI) is being used increasingly in various steps such as staging, assessing tumor response but also for treatment planning in radiotherapy [1]. The key to successful radiotherapy is to get a high local control of the disease while minimizing the side effects [2]. The first step, in doing so, is tumor definition and this is very critical and can be associated by large uncertainties [2]. The development of more sophisticated methods of modern radiotherapy such as intensity modulated radiotherapy (IMRT) and Tomotherapy increases the demand on an accurate determination of target and organ at risk volumes [1, 3].

The main reason for using MRI for treatment planning in radiotherapy lies in its superior soft-tissue contrast as compared to computerised tomography (CT) [1, 3]. The possibility of having several different imaging sequences, all providing various contrast, to visualize different tissues make it easier to differentiate boundaries of tumor infiltration to that of normal structures and can thus improve target delineation in radiotherapy [1, 2, 4]. MRI can in the same manner be of use to better define the volumes of organs at risk (OAR) [1, 3, 4]. Areas where MRI provides a better visualization and currently is used as a diagnostic tool for better delineation of target and OARs are the central nervous system (CNS) and the pelvis area (for example urological-, gynecological- and prostate-cancer) [1, 5]. Another advantage to MRI over CT is the ability of acquiring images in any plane and the ability to evaluate treatment response [1, 5]. The disadvantages concerning the utility of MR-images for treatment planning in radiotherapy is mainly its lack of electron density information and geometric distortions [2, 3, 5]. A common solution to the lack of electron density information from MRI has been to fuse CT- and MRI-images [3, 4, 6, 7]. The advantages with this approach are that the information about the soft-tissue from MRI, the electron density information and the visualization of bony structures can all be gathered [1, 6, 7]. The disadvantages are the uncertainties in the fusing process e.g. slightly different patient positioning between the imaging modalities and organ motions [1, 3, 6, 8]. The demand for geometric distortion correction to the MR-images remains since it could introduce a systematic error to the fused images and into the treatment plan otherwise [1]. A solution to the problem concerning the lack of electron density information in MRI-images has been to consider the images as homogenous or to perform image segmentation and assign different bulk densities to various segmented areas [1-3, 6].

In previous years several papers have been published concerning low-field MR systems with an open design. These systems have the advantage of imaging the patient in the true radiotherapy treatment position with patient fixation devices but the disadvantage is the low signal-to-noise ratio (SNR) and a poorer spatial resolution as compared to scanners of higher field strengths [1, 3]. The more recent papers have thus been concerning 1.5 and 3 T scanners [6, 7, 9].

1.1 The aim

The challenges for MRI-based treatment planning are, as described above, mainly due to the lack of electron density information and the distortions prone to MR scanners leading to geometric uncertainties hampering the dosimetric accuracy [2, 3]. Another disadvantage is the lack of signal from bone, at least using conventional pulse sequences [3]. Before treatment planning based solely on MRI can be used, there is a need for less time consuming segmentation, which could perhaps be solved by using

an ultra short time of echo (UTE) pulse sequence making detection of signal from bone possible.

The aim for this master thesis was hence to investigate if UTE images could be used for improving MR-based treatment planning. The thesis examines if segmentation of bone can be based on images of the head acquired with the UTE pulse sequence and evaluates what kind of dosimetric differences that can be expected from treatment planning calculations based on these images as compared to the CT-based treatment plans. This will also be compared against treatment planning calculations under the assumption that the head is homogenous, which has been a common approach in previous papers [1, 3, 7]. The work has been divided into three parts; 1) evaluation of system induced geometric distortions in MR images, 2) tissue segmentation based on UTE-images and 3) dosimetric evaluation of treatment planning based on the derived images.

2. Background

2.1 MRI

The basics for image generation in MRI is that the slice selection gradient in combination with a slice selective radiofrequency pulse will select the protons that will contribute to the signal [8]. The phase encoding procedure is commonly repeated by a stepwise increase in amplitude to achieve an entire image and the purpose of the frequency encoding is to cause protons at different locations in the imaging volume to have slightly different frequencies [8]. In the reconstruction process of the images the frequency and phase information is used in the Fourier transform to retrieve different spatial positions [8]. Any change in these magnetic fields, such as a non-homogeneous B_0 or a nonlinearity in G , will thus lead to a displacement in space [8].

The clinically most used pulse sequences in MRI are T1-weighted (T1W) and T2-weighted (T2W) spin echoes (SE) or fast spin echoes (FSE) [10]. The T1W images give information about the anatomical structures of the patients and make it possible to visualize pathologies where the T1 is altered [10]. Similarly T2W images make it possible to detect pathologies characterized by an increase or decrease in their T2 components [10].

2.2 Image distortions

Data used by the treatment planning system should have minimal effects from image distortions since these will result in systematic errors in the positioning of tissues and as a consequence could cause dose calculation errors [2]. There is therefore a need to quantify and correct for these distortions and establish any possible effects on the dosimetric accuracy [2]. Several studies have stressed the importance of considering and measuring geometric distortions in MR-images [5, 6, 11]. The aims have been to evaluate and reduce the geometric distortions to less than 2 mm, a generally accepted requirement in radiotherapy, through different corrections and to test the robustness of the used correction method [5, 6, 12].

The geometric distortions in MRI-images are commonly divided into two groups: object-induced effects and system-induced effects [1, 3, 6, 8, 9].

2.2.1 Object-induced distortion

Object-induced effects are distortions that arise when the magnetic fields are altered by the object itself and include chemical shift and susceptibility effects [1, 5, 6, 8]. These effects generally increase with increasing field strength and decreases with increasing imaging bandwidth, though the latter is also leading to a decreased SNR [8].

Chemical shift occurs as a result from the fact that protons are differently bound to molecules in fat-tissue and hence have a slightly different resonance frequency as compared to protons in water-like tissue [1, 8]. The difference in resonance frequency cannot be resolved by the spatial encoding process, and hence causes the fat to be mispositioned in the frequency encoding direction [8, 9]. The displacement caused by chemical shift increases with increasing B_0 since the difference in resonance frequency then becomes greater if the bandwidth of the readout gradient is unaltered [8].

Susceptibility effects arise from objects having different magnetization properties, leading to local changes in the magnetic field [8, 9]. The changes of the magnetic field causes the signal from the affected area to become out-of-phase and consequently to be misinterpreted by the Fourier transform resulting in a geometric displacement [8-10]. Susceptibility effects are evident at the interface between two materials with different susceptibility, such as tissue/air and tissue/bone interfaces [1, 8].

2.2.2 System-induced distortion

System-related effects mainly concern inhomogeneities in the scanners' static magnetic field (B_0), gradient (B_{grad}) non-linearity and eddy currents [1, 8].

The need to correct for system-related distortion in MRI has again become more of an issue since the development of short-bore magnets and because of the new generation of gradient systems where the demands of fast rise times (slew rates) have resulted in shorter gradient coils [11, 13]. The shorter length of the gradient coils and the fewer turns can lead to the consequence of increasing nonlinearity in the gradient field [8, 11, 13, 14]. Usually system-related distortions increase with distance from the centre of the magnet bore and are thus largest in images with a large FOV [1, 8]. The system-induced distortions can be expressed as [8]:

$$\Delta z = \Delta B_{\text{grad},z}(x,y,z)/G_{\text{slice}} + \Delta B_0(x,y,z)/G_{\text{slice}} \quad (1)$$

$$\Delta y = \Delta B_{\text{grad},y}(x,y,z)/G_{\text{phase}} \quad (2)$$

$$\Delta x = \Delta B_{\text{grad},x}(x,y,z)/G_{\text{read}} + \Delta B_0(x,y,z)/G_{\text{read}} \quad (3)$$

G denotes the gradient strength for the chosen direction, i.e. with index = x, y or z being equal to slice, phase and frequency encoding directions [8]. $\Delta B_{\text{grad},\text{index}}$ with the same indexing describe errors in the gradients and ΔB_0 denotes errors in the static magnetic field [8]. .

Wang *et al.* investigated the distortions for four 1.5 T MRI scanners and the differences obtained with and without applying the vendors' distortion correction [11]. They found that, for a 3D T1W spin echo sequence, the system-induced

distortions could be reduced by 20 %- 80 % with the vendors' distortion correction and that the remaining distortion was less than about 2.5 mm within a spherical volume of 3.6 dm³ but as much as 7 mm within a cubic volume of 13.8 dm³. The correction was only performed in the imaging plane (2D) and the distortion along the slice selection direction was hence unaffected with values of up to 9.7 mm for the larger volume but remained fairly small, less than 2 mm, within the smaller volume.

Doran *et al.* evaluated the system induced distortion in 3D in a 1.5 T MRI scanner by comparing images of a phantom acquired with a CT to those acquired with MRI [13]. The authors investigated the system-induced distortions within a volume of 440×270×360 mm³ with a 3D gradient echo pulse sequence. In the third dimension, the through plane, distortion was seen in the images. Doran *et al.* found system-induced distortions of more than 1.875 mm (one voxel) in 25 % of the investigated points and system induced distortions of more than 10 mm in 5 % of the points within the volume. They explained some of these distortions to be a result of the points not being mapped correctly by their method. Reducing the volume to 365×230×340 mm³ resulted in that only 1 % of the voxels had distortions above 1.875 mm although these distortions could be as large as 25 mm. All values above are for the x-component of the distortion but the authors claimed that the similar figures could be generated for the other directions.

2.2.3 Phantom used to evaluate geometric distortions

System related distortions are best quantified and corrected for using a phantom with markers that can be located in three dimensions (3D) [1, 8, 14]. There are two important requirements to consider when using a phantom for quantification of the system-induced distortions; the phantom needs to have enough control points to be able to map the variation of the distortions adequately and the control points need to be well defined in order to provide a correct quantification of the distortions [14]. Markers positioned at the periphery or at the surface of a patient can provide a measure of the object-induced distortions [1, 5]. Wang *et al.* used a cubic phantom, 310×310×310 mm³, consisting of different planes defining positions in 3D [11, 14]. The planes were made of plastic sheets and the phantom was water-filled [14]. Doran *et al.* used a 440×270×360 mm³ linearity test-object phantom consisting of orthogonal rods [13]. The majority of the phantom consisted of air but the orthogonal polymethylmethacrylate (PMMA) tubes were filled with water [5, 13]. The phantom used in the studies by Wang *et al.* had 381 points per plane with a total of 10 830 control points whereas the phantom used in the study by Doran *et al.* had 84-132 points per plane depending on which of the planes that was being imaged, with at total of number of control points being between 16 757 and 7115 [13, 14].

2.3 UTE pulse sequences

As already stated the use of UTE pulse sequences in MRI could solve the need for faster segmentation of bone before assigning different bulk densities to various areas used for the dose calculation [9]. Another use for UTE pulse sequences is that they would possibly give the opportunity to make MRI digitally reconstructed radiographs (DRR). These are projection images that help verifying patient position at the linear accelerator by matching visible structures seen in x-ray images or MV-images taken using the accelerator at treatment, with those seen in the DRR [2, 4, 9].

In MR images from clinically used pulse sequences, bone and other tissue with short T2 relaxation appear dark, with signal fully relaxed before image acquisition has

begun [10, 15]. Cortical bone has a T2 of 0.4-0.5 ms and T1W and T2W SE or FSE have a TE of 8-200 ms, hence bone has no signal in those images [10, 16]. Even with gradient echo sequences (GRE), that can have shorter TEs of about 2 ms, this is still not short enough to detect signal from cortical bone [10].

One single type of tissue can have several different T2 components but usually they can be divided into two groups; tissue with a minority of short T2 components or tissue with a majority of short T2 components, where bone is in the latter [10, 15, 16]. The differences in T2 reflect differences in how the protons are bound to other molecules and differences in neighboring atoms [10, 16]. Strong dipolar interaction between tightly bound protons in solids and crystals is one mechanism that leads to short T2 and another leading to short T2 is the susceptibility effects previously described [10]. Solids are characterized by broad spectral lines, due to their short T2-relaxation as compared to conventional MR-imaging of solutions with longer T2 and narrow spectral lines [10, 15]. This broad bandwidth of short T2 components complicate the use of fat saturation pulses and long T2 saturation pulses since these pulses result in off-resonance effects of the short T2 components and thereby reduce their signal [10]. With T2 being shorter or of about the same length as the duration of the radio frequency (RF) pulse, the relaxation mechanisms dominate [10, 15]. The RF pulse exciting the protons in the selected slice hence becomes a competition between the rotation of the magnetization vector into the transverse plane and the relaxation of the excited spins [10]. The effect is a reduction of the magnetization as compared to the expected with the applied flip angle [10]. The 2D UTE pulse sequence therefore generally consists of two halves of RF pulses exciting the protons [10]. Both times, the slice gradient is applied simultaneously, differing only in the polarity [10, 15]. The signal is typically read into k-space in a radial manner by ramping of the gradients, starting at zero until reaching a plateau [10, 15]. This is done between each excitation pulse and the signals from the two halves of RF pulses add up to produce one line in k-space [10, 15]. The UTE signal is not really an echo but a sampling of the free induction decay (FID), hence adding the two FIDs generated by the two RF excitations bring the signals in phase [16]. A further reduction in TE can be achieved using a non selective 3D block pulse and instead of the slice selection gradient use the coil's sensitivity profile for slice selection [15]. This is followed by a collection of the signal by ramping of the gradients just as in the 2D sequence but now in 3D, forming a sphere in k-space [15]. A disadvantage of radial acquisition is that it is rather ineffective with an imaging time for radial collection of signal π times longer as compared to a Cartesian data collection [15]. However, the over sampling of the center of k-space results in higher SNR [15].

To visualize the short T2 components, it is further needed to reduce the signal from components of longer T2 [10]. Such methods are either dephasing of the long T2 components with crusher gradients, using an inversion pulse to cancel the long T2 components or by subtracting a later echo from the shortest, thereby enhancing the components with the fastest decaying signal [10]. The latter is, by some authors, stated to be sensitive to susceptibility artifacts and to give an increase in image noise, generated by subtraction of the two echoes, but it still seems to be a rather common method for *in vivo* imaging [10, 16]. The disadvantage with applying additional pulses is a reduction of the signal as described above [10].

2.4 External radiotherapy

Two of the most fundamental demands in radiotherapy treatment planning is the need for geometrically correct images to delineate target and OARs accurately and information about the electron density of tissues in the images used for treatment planning in order to make a correct calculation of the dose distributions [1]. CT is the modality of choice since it fulfills both these demands [1].

2.4.1 Treatment delivery techniques

The aim in radiotherapy is to deliver a high dose to the target area and a low dose to the surrounding tissue [4]. In 3D conformal radiotherapy (3D CRT) the beam is shaped in the beam's eye view (BEV) using multi leaf collimators (MLC) and the jaws [4]. The BEV is only a projection of the target at each chosen angle of beam delivery and therefore no concave dose distributions can be achieved [4]. The desired dose distribution is obtained by varying the number, weight and shape of the beams [4]. This is performed by the planner and is called forward planning [4]. IMRT is an alternative delivery technique using modulated beams, enabling concave dose distributions to be delivered [4]. The technique uses inverse planning where the beams and non-uniform dose intensity profiles are calculated from the desired dose distribution [4]. Altering the weight of the individual elements of each beam, called beamlets, produces the non-uniform dose intensity profiles [4]. This calculation is an iterative process thriving to fulfil the set dose criteria to target and different OAR through penalties weighting the importance between these structures [4]. The beamlets leading to the non-uniform dose intensity profiles are delivered at the linear accelerator through controlling the motion and/or position of the MLC [4].

2.4.2 CT-based treatment planning

CT is used both for tumour diagnosis and for radiotherapy treatment planning [2]. It does not suffer from any distortions and the physics is well known, which has made it by far the most common modality in this area [2, 4].

The images acquired with a CT-scanner are derived from back projections of the attenuation of the x-rays in the irradiated tissue [2, 4]. The signal intensities in the CT-image are given as Hounsfield units and describe the relationship between the linear attenuation coefficient for the scanned area and the linear attenuation of water for the photon energy used in the CT [4]. The linear attenuation coefficient is a product of the electron density and the electron cross section [4]. By combining these two relationships equation 4 can be obtained [4]:

$$HU = \frac{1000(\rho_{et}\sigma_{et} - \rho_{ew}\sigma_{ew})}{\rho_{ew}\sigma_{ew}} \quad (4)$$

where ρ_e denotes the electron density for water (ρ_{ew}) or tissue (ρ_{et}) and σ_{ew} and σ_{et} denote the electron cross section for these materials [4]. This can be rewritten as:

$$HU = \frac{1000 \cdot (\frac{\rho_{ew}}{\rho_{et}} - R)}{R} \quad (5)$$

$$R = \frac{\sigma_{ew}}{\sigma_{et}} \quad (6)$$

where R is a ratio of electron cross sections for the two materials [4].

Equation 5 describe how the Hounsfield units can be converted to electron densities for the chosen energy and these relations are stored in a look-up table in the treatment planning system and should be checked regularly with a CT calibration phantom consisting of material with different electron densities [2, 4]. The electron densities for the various tissues in the images acquired by the CT are used by the treatment planning system for calculating a dose distribution by determining the attenuation of the beam within each tissue and correcting for inhomogeneities [2, 4]. The CT-data are also used for creating DRR by the treatment planning system [2].

2.4.3 MRI-based treatment planning

At the University Hospital in Lund, MRI is used only as a complement to CT-images when the extension of the tumor is difficult to depict in the CT-images. Examples of such areas are CNS, head & neck and prostate.

At this stage there is a potential for treatment planning using solely MR-images, at least in areas with high tissue homogeneity [2]. However, no simple relationship between the intensities of different tissue in the MR-images to the electron density values exists [1, 6, 8]. Instead, to be able to solely use MR-images for treatment planning in radiotherapy one needs to assign bulk densities to tissues after segmentation [1, 6, 8]. In areas characterized by large tissue inhomogeneities, such as the head and neck, segmentation and the assigning of bulk densities might be difficult and time consuming [1]. Studies of MRI-based treatment planning have usually focused on homogeneous areas such as the brain or as in the majority of the studies, the prostate [2]. These studies have often assumed the electron density of water to the entire brain or pelvis area [1, 2, 8]. More recent studies have tried to segment bone and apply a different bulk density, to for example, the skull [6, 9].

Stanescu *et al.* have in two papers focused on intracranial lesions treated with IMRT consisting of five beams [6, 7]. They investigated the dosimetric accuracy achieved with MRI-based treatment plans as compared to those calculated from CT-images for four glioblastoma multiforme patients. The 3D MR-images (T1W and T2W) were acquired on a 3 T scanner about half an hour after the CT-scan, with the same patient positioning devices [6]. The T1W fast gradient echo images were used for drawing the target [6]. Using both the T1W and the T2W MR-images, bone were segmented and, after distortion correction, the MR-images were assigned bulk densities of water (1 gcm^{-3}) in brain-tissue and scalp areas and that of bone (1.47 gcm^{-3}) for the skull [6]. The same contours (target and OAR), beam arrangement and photon fluences as in the original CT-based treatment plans were also used for the derived CT plans (with assigned bulk densities) and for the MRI-based treatment plans [7]. The impact of assigning bulk densities was investigated by comparing CT treatment plans based on the original CT-data to those plans based on bulk densities assigned to the same areas as in the MR-images [6]. The difference in dose to isocenter and the mean, maximum and minimum dose in PTV were all less than or equal to 1 % when comparing these plans [6]. When comparing the dose volume histograms (DVH) for these treatment plans Stanescu *et al.* found no clinical difference. As for the MRI-based treatment plans the difference in dose to isocenter and the mean and maximum dose to PTV were all less than 1.9 % in comparison to the CT-based treatment plans [6]. The minimum dose to PTV differed more, ranging from 4.7 % to 12.5 %, for the four patients [6]. These differences could be seen in the DVH as well [6]. On the basis of their data Stanescu *et al.* concluded that the MRI-based treatment plans were suitable for radiotherapy.

3. Methods

3.1 Evaluation of distortion

As a first step toward treatment planning based on MR-data alone, one needs to quantify any geometric distortions, which depend on both the scanner and the pulse sequence being used [6, 11]. Comparing CT-images of the phantom to those acquired with MRI made an evaluation of the distortion at given positions in the phantom possible. Such a comparison can be performed using e.g. MatLab. The method assumed that the CT-images are free from any distortions.

3.1.1 Phantom used for the measurements

The cylindrical phantom used for evaluating the distortions was made of PMMA and was filled with water. The length and the outer diameter of the phantom were both 18 cm and within this volume 89 rods of PMMA were positioned in a well-defined grid. The rods had a diameter of 3 mm and were separated 15 mm from one another. Small surgical plastic tubes filled with diluted MRI contrast agent (Dotarem $279.3 \text{ mg}(\text{ml})^{-1}$ gadolinic acid) and D-vitamin tablets were fixed on the phantom, in order to help locate the middle slice of the phantom in the acquired images. These surgical tubes, without the MRI-contrast agent, are used for radiotherapy treatment planning at the Oncology department in Lund when marking the reference points in CT-scans of head patients.



Figure 1. Image of the phantom used for evaluation of the distortion.

3.1.2 Image acquisition

The phantom was positioned in both the CT and the MRI scanner by guidance of each system's orthogonal lasers. The middle of the phantom was located close to the isocenter of the MRI-scanner.

The CT-scanner used was Siemens Sensation Open and some of the parameters for the scan are shown in table 1. In MRI, all imaging were acquired using a Philips Achieva 3T scanner with the Sense-Flex-large coil.

Three MR imaging sequences were investigated with consideration to system-induced distortions; a T1W 2D-SE, a T2W 2D-FSE and a 3D dual echo UTE pulse sequence. These are sequences of interest because they are what clinically could be used to gain information both on the extension of the tumor as well as the different anatomical structures of the brain. For the T2W FSE an echo train length (ETL) of 15 was applied. Other imaging parameters used for the MRI scanning are shown in table 1.

Optimization of the appropriate delayed reconstruction times was conducted prior to performing measurements with the UTE-pulse sequence. A more detailed description of execution is given in section 3.2.

To evaluate any geometric distortion related to the imaging gradients, the phantom was rotated so that the tree physical gradient directions (x, y and z) were used for different imaging encodings (slice, frequency and phase encoding). This was conducted so that the positions were seen when imaging axial slices i.e. using the system directions X and Y for frequency and phase encoding directions, sagittal slices i.e. using the system directions Y and Z for frequency and phase encoding directions and coronal slices i.e. using the system directions X and Z for frequency and phase encoding directions slices. Two scans were collected for each SE or FSE sequence; one with the manufacturer's distortion correction turned on and one when it was turned off. To make the matching of the images more reliable, a homogeneity correction was applied to the SE- and the FSE-pulse sequences, making the image intensity more homogenous throughout the images. The homogeneity correction enabled almost all the rods in every image slice of the phantom to be detected and made simple thresholding of the image intensity feasible.

Table 1. Scanning parameters for the evaluation of the system induced distortions.
*Field of view (FOV)

	CT	MRI		
		T1W SE	T2W FSE	UTE
Matrix [pxl]	512 × 512	400 × 400	400 × 400	336 × 336
FOV* [mm]	200 × 200	200 × 200	200 × 200	300 × 300
Slice thickness [mm]	3	3	3	0.90
Pitch	1	-	-	-
(TE/TR/Flip angle) [ms/ms/°]	-	(11/500/76)	(80/3000/90)	(0.08/9/20)

3.2 The UTE pulse sequence

All imaging of the volunteers was performed using a Philips Achieva 3T scanner. The dual echo 3D UTE sequence used in this work gather the data in a spherical geometry, denoted kooshball. The radial collection of k-space was reformatted to Cartesian coordinates before the Fourier transform.

To be able to achieve echo times shorter than 0.1 ms the Sense-Flex-large coil was used. This coil has a fast switching between RF transmit and signal receive mode, which sets the limitation for the shortest TE achievable [17]. Additionally, to be able to use the short echo times, a special coil patch needed to be installed, which was performed with help of a clinical scientist engineer from Philips.

Before imaging with the UTE pulse sequence, a calibration of the trajectory delay was conducted. Determining the delayed reconstruction time will ensure a better image quality since this time compensates for possible time differences in actual and

expected collection of signal in the coil [17]. The delayed reconstruction time was determined by collecting image raw data of the phantom described in section 3.1.2. The raw data of the phantom was then reconstructed with different delayed reconstruction times, ranging from $-5 \mu\text{s}$ to $5\mu\text{s}$. The reconstructed images were evaluated considering the best definition of the edges of the phantom and the corresponding time for delayed reconstruction was chosen and used for online reconstruction in all further imaging using the UTE pulse sequence.

Four volunteers were imaged, after their informed consent, with the 3D dual echo UTE pulse sequence with the first TE at 0.08 ms and the second TE at 4.6 ms. The images were subsequently used for segmentation of bone, air and soft tissue. Parameters for the pulse sequence used are displayed in table 2.

Table 2. Scanning parameters for the four volunteers.

Volunteer	Reconstruction matrix [mm]	TR [ms]	Flip angle [°]	Pixel bandwidth [Hz]	Slice thickness [mm]
1	224 × 224	7.5	20	1343	1.51
2	224 × 224	8	20	1420	1.60
3	224 × 224	8	20	1420	1.56
4	224 × 224	8	20	1420	1.56

3.3 Image post processing

3.3.1 Matching of the images for evaluation of distortion

The matching of the images was performed using code written in MatLab. To reduce the uncertainties in the positioning of the phantom between the two modalities the middle slice in the CT-images of the phantom was used as a template for matching. The MatLab function BWlabel was used to search the image for areas with similar intensity, which in these images were the 89 rods appearing as circular areas (dots) in the images. The center of gravity for the area categorized as a dot for every dot found in the MRI-images was compared to the ones found in the CT-template. Before comparison of these center of gravity values, the position of the dot located in the center of the phantom in the middle slice of the MRI-images was matched to the same location as the corresponding dot in the CT-template. This was done under the assumption that the central position in the MR images does not suffer from any distortions. For the CT-template an edge detection filter was applied before using BWlabel to find the positions since this was seen to reduce the variation of the values of center of gravity within the template.

3.3.2 Segmentation

The segmentation of bone and air from the images were performed in MatLab. Using data from the two echoes together with the data from images produced by subtraction of the two echoes (subtraction map) the bone together with air was segmented. In the images of the shortest echo time, tissues with short T2 have high signal intensity and

air has low intensity whereas in the second echo, tissues with short T2 has been phased out and hence have an intensity value similar to air. This information was used to segment air through thresholding low intensity (below 20) in the first echo. Bone signal was segmented adding areas created from thresholding low intensity values (below 40-50) in the second echo to areas created when thresholding high intensity values (above 25) in the subtraction map. An edge detection filter was applied in order to reduce the overestimation of areas segmented as bone in the periphery of the head. The outer edges of the image received after edge detection filtering was widened. This widened area was then subtracted from the image segmented as bone obtained through the thresholding of the intensity, as described above.

The segmentation of bone was performed in a standardized manner for all four volunteers, only varying the intensity thresholding slightly. Both the pixels segmented as bone and the pixels segmented as air was written to the subtraction map and assigned low and high intensity values respectively before being rewritten to the Digital Imaging and Communications in Medicine (DICOM) format.

3.4 External radiotherapy treatment planning

All treatment planning was performed in Oncentra Masterplan (OMP). Already existing treatment plans in OMP from 12 patients with tumours located in the head and neck area were investigated. Nine of the patients had existing 3D CRT and three of the patients had existing IMRT plans. Eleven of the twelve patients had brain tumours and one had a tumour to the nose including three targets (patient # 10). Some parameters for the twelve cases are listed in table 3.

To evaluate what variation in dose to be expected from plans generated from MRI-image data, CT-images were derived to resemble MR-images by generating different ROIs with assigned densities, in literature denoted bulk densities. In the treatment planning system three ROIs were generated: one containing pixels of bone, a second containing pixels of air and a third containing pixels of soft tissue. The latter was produced by subtraction of the external contour with the ROI of bone and the ROI of air. Both pixels considered to image bone and pixels considered to image air were found using the function “magic wand” in OMP. “Magic wand” is a function that uses similar intensities in the image to create a ROI, and this was performed slice by slice for all CT-data of the included patients. After creating these ROIs a density value of 1.610 gcm^{-3} was assigned to the ROI of bone, a density value of 1.025 gcm^{-3} to the ROI of soft tissue and a density value of 0.001 gcm^{-3} to the ROI of air. The value for soft tissue was a mean value of soft tissue for men and women based on ICRU 46 [18] and the value of bone was for Skeleton Cranium taken from the same source. The value for air was taken from literature [9].

For each patient two additional sets of treatment plans were generated, one containing the bulk density plan which further will be denoted $\text{Plan}_{\text{UTESim}}$ and the other plan created based on assuming the entire CT imaged volume to be homogenous with the density of water which will be denoted $\text{Plan}_{\text{MRISim}}$. Every plan was calculated in OMP using a pencil beam algorithm and with all other parameters identical to the original plan. For the IMRT plans, the optimization calculated from the original plan was used to make the final dose calculation for this plan as well as for the two additional plans. As a second evaluation of the derived plans, new optimizations followed by a final dose calculation were made for each of these plans. $\text{Plan}_{\text{UTESim}}$ and $\text{Plan}_{\text{MRISim}}$ were compared against the original treatment plan with respect to minimum, maximum and mean dose to PTV, isodoses, DVH and maximum dose to OAR. The minimum and

maximum values are for those voxels where over 0.5 of the voxel is included by the particular ROI [19].

Table 3. Parameters for the treatment plans of the 12 patients

Patient number	Volume of PTV [cm ³]	Dose per fraction [Gy/fr]	Number of fractions	Number of treatment fields
1	434	2	28	3
2	377	2	29	4
3	733	3.4	10	2
4	447	5	5	3
5	327	2	29	4
6	104	2	25	3
7	402	2	28	3
8	378	2	29	4
9	582	3.4	10	2
10	343	2	23	7 (IMRT)
	227	2	23	7 (IMRT)
	229	2	23	7 (IMRT)
11	815	1.8	30	7 (IMRT)
12	516	1.8	31	7 (IMRT)

4. Results

4.1 Image distortions

In figure 2, a CT- and a MR-image of the phantom used is shown.

Regarding MRI, the system-induced distortions were similar when the phantom was separately imaged in all three directions. Due to this fact, only plots of one of the directions and one pulse sequence (T1W SE) tested are shown below. Plots from the other pulse sequences can be found in Appendix. The plots included data for coordinates x and y for the first, the middle and the last slice as the distortions were expected to be worse further away from the MRI scanner isocenter due to gradient linearity and field inhomogeneity [8]. For the same reason, in figure 5 the outer positions of the phantom, marked with corresponding numbers in figure 2 were plotted as a function of slices.

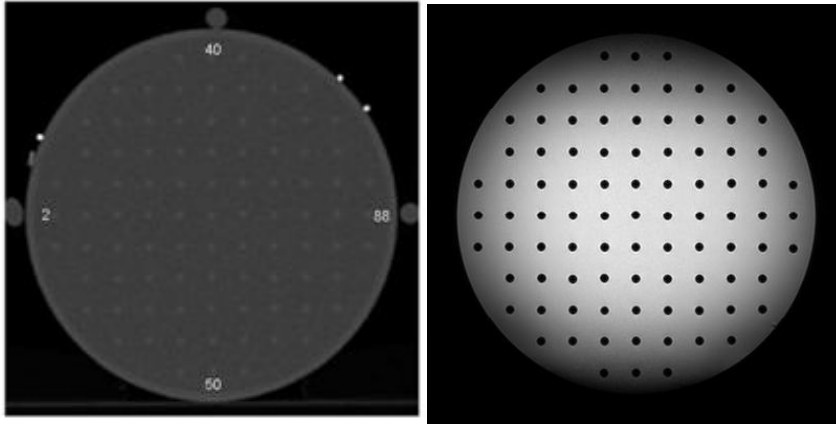


Figure 2. To the left a CT-image of the phantom used for evaluation of the distortion and to the right a T2W MR-image of the phantom.

In table 4-6 the absolute maximum distortion was calculated as:

$$r = \sqrt{x^2 + y^2} \quad (7)$$

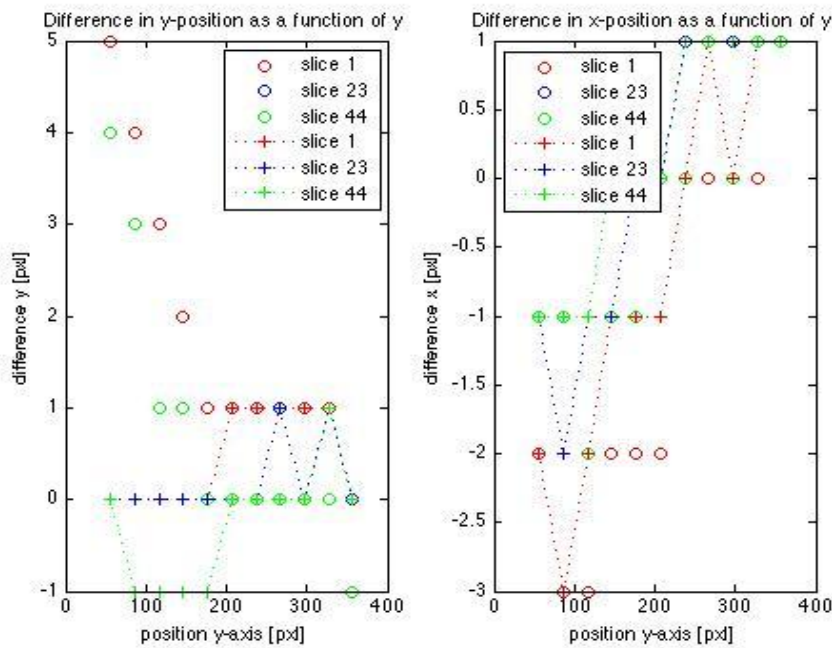


Figure 3. Difference in the coordinates in the anterior-posterior direction for the TIW pulse sequence. Measurement with the vendor's distortion correction applied is denoted with crosses whereas measurement without any distortion correction applied is denoted with circles.

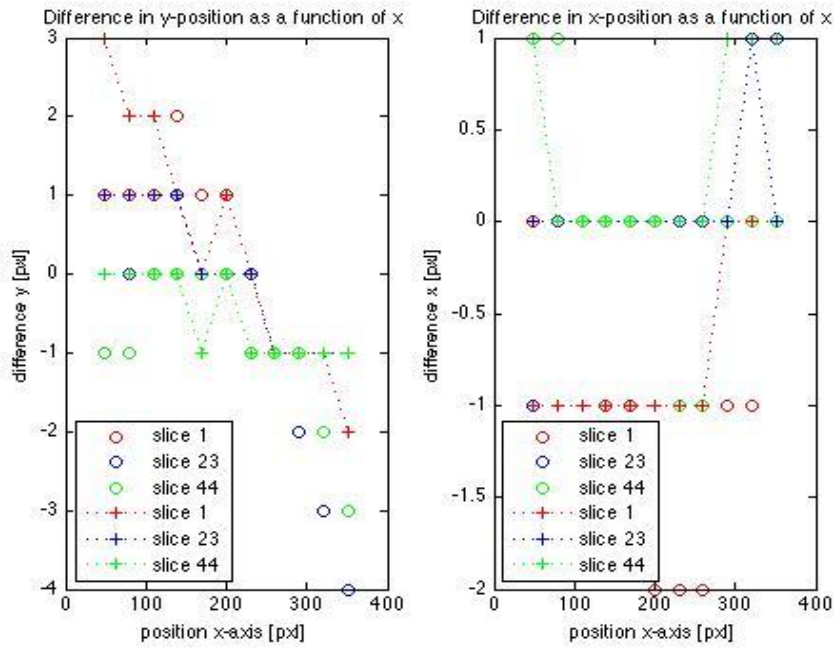


Figure 4. Difference in the coordinates in the dextral-sinistral direction for the TIW pulse sequence. Measurement with the vendor's distortion correction applied is denoted with crosses whereas measurement without any distortion correction applied is denoted with circles.

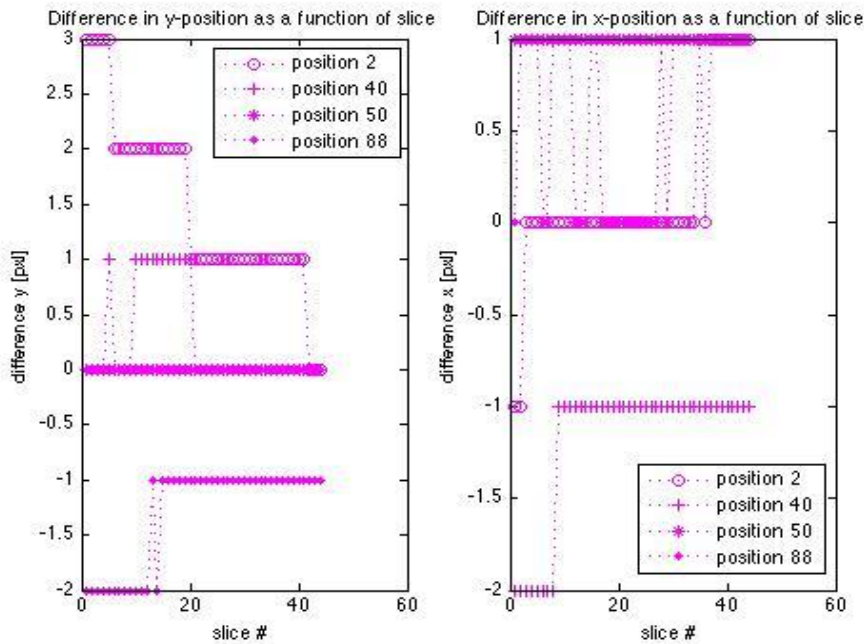


Figure 5. Difference in the coordinates as a function of slice in the cranial-caudal direction for the TIW pulse sequence. Only measurement with the vendor's distortion correction applied is shown.

Table 4. Data over the system-induced distortions with the phantom positioned such that the 89 dots appear when imaging axial slices, i.e. using the system directions X and Y for frequency and phase encoding directions

Pulse sequence		Absolute max distortion [mm]			
		r	X-direction	Y-direction	mean
T1W SE	with correction	4.6	4.5	4.5	1.5
	W/O correction	5.1	5	4.5	1.6
T2W FSE	with correction	1.6	1.5	1	0.2
	W/O correction	3.5	3.5	2.5	0.4
UTE with distortion correction		2	1.8	0.9	0.7

Table 5. Data over the system-induced distortions with the phantom positioned such that the 89 dots appear when imaging sagittal slices, i.e. using the system directions Y and Z for frequency and phase encoding directions

Pulse sequence		Absolute max distortion [mm]			
		r	Y-direction	Z-direction	mean
T1W SE	with correction	1.6	1.5	1.5	0.4
	W/O correction	2.7	2.5	2	0.5
T2W FSE	with correction	2.6	1.5	2.5	0.4
	W/O correction	3.2	1.5	3	0.5
UTE with distortion correction		6.8	6.3	2.7	0.7

Table 6. Data over the system-induced distortions with the phantom positioned such that the 89 dots appear when imaging coronal slices, i.e. using the system directions X and Z for frequency and phase encoding directions

Pulse sequence		Absolute max distortion [mm]			
		r	X-direction	Z-direction	mean
T1W SE	with correction	2.5	1.5	2	0.5
	W/O correction	2.5	2.5	2	0.6
T2W FSE	with correction	2.1	1.5	2	0.6
	W/O correction	2.9	2.5	2	0.7
UTE with distortion correction		2.5	1.8	1.8	0.7

4.2 The UTE pulse sequence

Images acquired with the UTE pulse sequence for one volunteer are displayed in figure 6. The figure shows images of both echo times as well as the subtraction map.

The images corresponding to the shortest echo time showed lack of contrast and not only bone appeared as high-intensity signal. Areas corresponding to low-intensity signal in the short-TE images were considered to be areas containing air. In the images corresponding to the second echo, both areas containing air as well as tissue with short T2 appeared as low-signal intensity areas. The images from the second,

longer TE, showed a larger contrast as compared to the first echo. The visualization of bone was enhanced in the subtraction map but high signal intensity areas were also seen for the periphery of the head and other areas. In the subtraction map tissues with longer T2 values were cancelled.

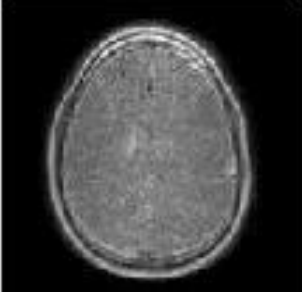
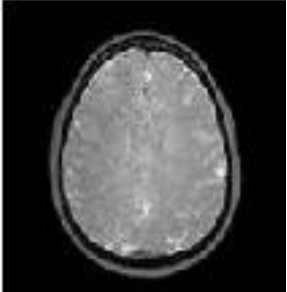
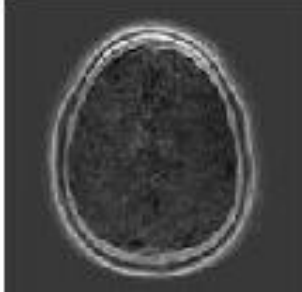
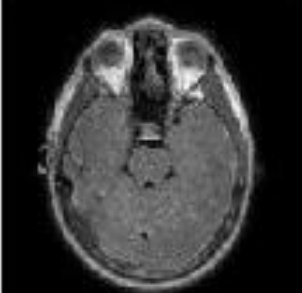
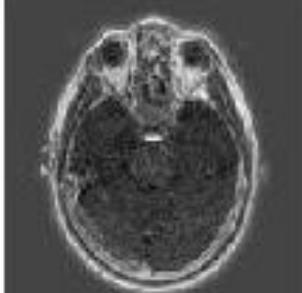
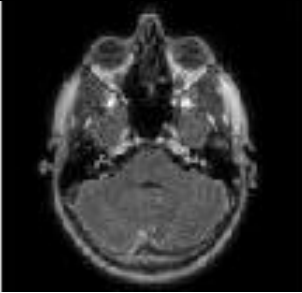
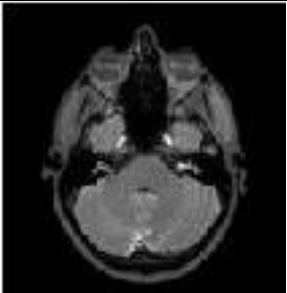
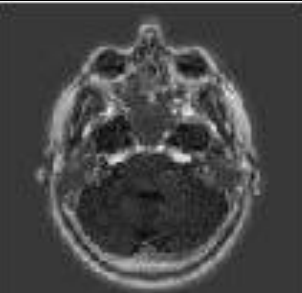
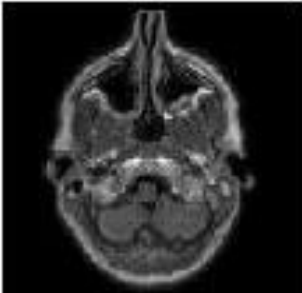
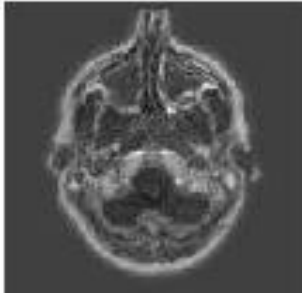
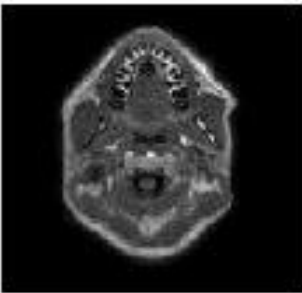
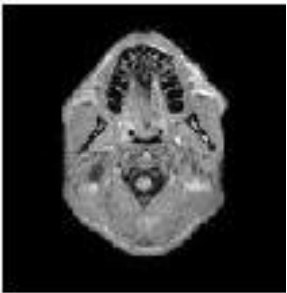
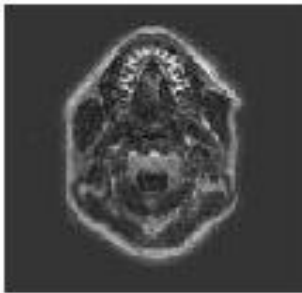
TE1 = 0.08 ms	TE2 = 4.6 ms	Subtraction map (TE1-TE2)
		
		
		
		
		

Figure 6. Images of different slices for volunteer 4 acquired with the 3D dual echo UTE pulse sequence.

4.3 Segmentation of bone and air in the head

Images acquired with the 3D dual echo UTE pulse sequence, where bone and air have been segmented are displayed in figure 7 for the four volunteers. Segmentation of bone based solely on thresholding pixels with high intensity values in the subtraction map lead to an erroneous categorisation of the periphery of the head as bone. In this work, this issue/probem was solved by both including information from the second echo and by applying an edge detection filter on the images of this echo. In figure 7 bone has been assigned a high intensity value of and appears white whereas air has been assigned a low intensity value and appears black within the skull. The intensity values for the remaining tissues were unaltered. A slight difference in the anatomy of the head of the volunteers could be seen. In a few slices the periphery of the head was still categorized as bone. For volunteer number two, the imaging volume and the head were not properly aligned, hence the head seeming to be somewhat tilted.

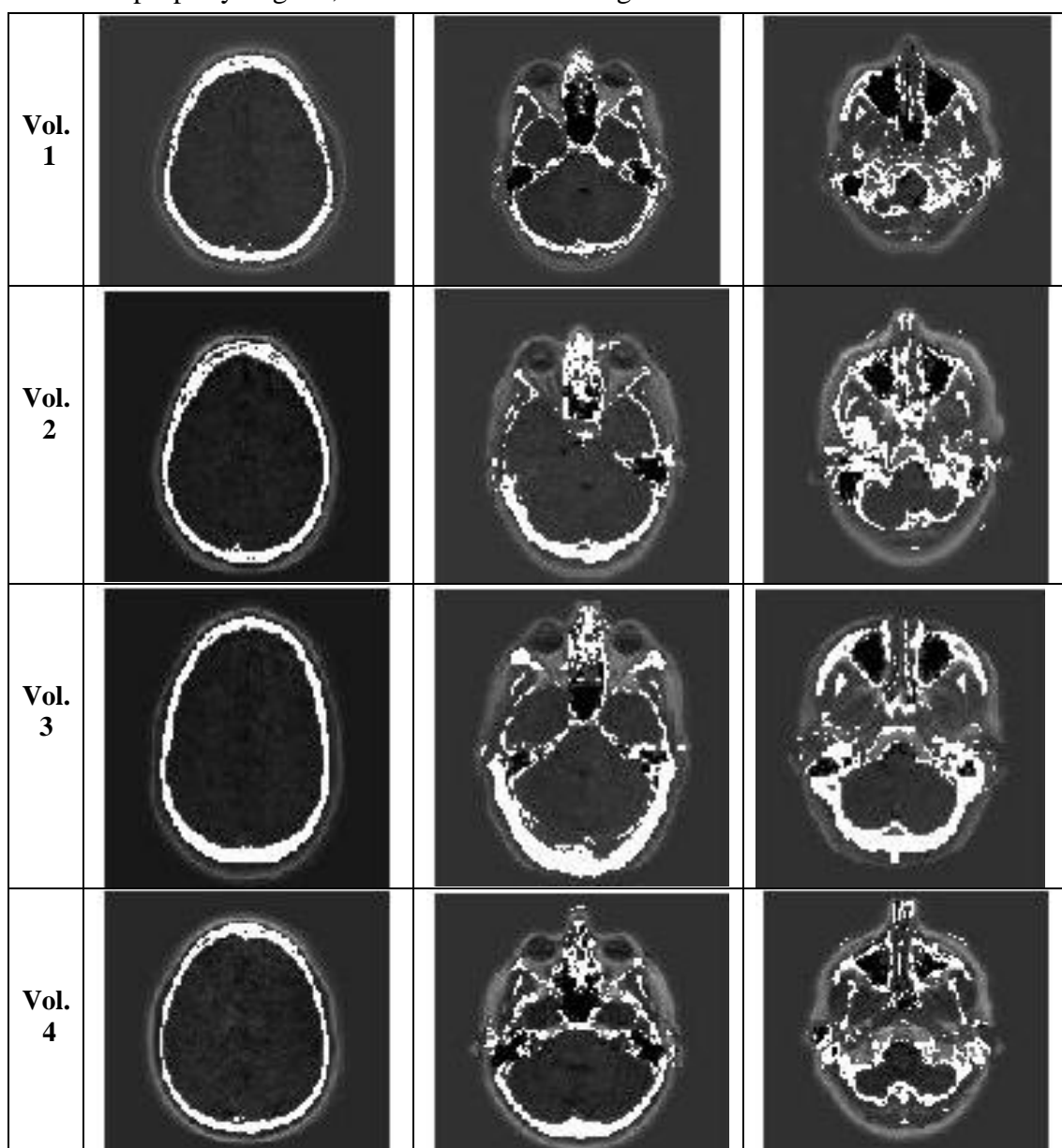


Figure 7. Segmented images of the UTE pulse sequence for the four volunteers. The slices shown are chosen to be at the same distance with respect to the beginning of the scalp. For the first column this distance is about 5 cm, the second column about 11 cm and the third column about 13 cm from the scalp, respectively.

The total volume of the segmented tissues, for approximately the same imaged volume and with similar location, is displayed for all volunteers in table 7. The comparison for bone was made for a distance of about 17 cm, starting at the beginning of the scalp. The corresponding distance for air was about 12 cm. For all volunteers a mean volume of 530 cm³ and 71 cm³ were segmented as bone and air respectively.

Table 7. Segmented tissue volumes for the four volunteers.

Volunteer	Segmented tissue [cm ³]	
	Bone	Air
1	458	88
2	481	52
3	660	62
4	521	81

4.3 Treatment planning with bulk densities

4.3.1 3D CRT

For the conformal treatment plans (patient number 1-9) the mean dose to PTV were very similar to the original plan for both Plan_{UTESim} and Plan_{MRISim}, with a total mean value of the difference in percentage of -0.11 ± 0.12 % and -0.15 ± 0.20 %, respectively. The mean of the difference in maximum dose to PTV expressed in percentage were -0.35 ± 0.63 % for Plan_{MRISim} and -0.09 ± 0.25 % for Plan_{UTESim}. The corresponding mean values for the difference in minimum dose to PTV expressed in percentage were 0.02 ± 1.44 % and -0.20 ± 0.98 %. The mean doses to target were slightly underestimated in all patients for both the segmented plans and the water approximated plans as compared to the original plan, as seen in table 8 and 9.

Table 8. Mean, minimum and maximum dose to PTV given in Gy.

Patient number	Mean dose (min – max) [Gy]		
	Original CT	Plan _{MRISim}	Plan _{UTESim}
1	56.40 (52.09-60.53)	56.36 (52.32-60.45)	56.23 (52.05-60.47)
2	58.25 (51.00-63.05)	58.08 (51.00-62.44)	58.13 (50.89-62.80)
3	34.36 (32.79-35.44)	34.44 (32.32-35.08)	34.30 (32.69-35.42)
4	25.28 (22.64-26.51)	25.19 (22.57-26.23)	25.26 (22.74-26.47)
5	58.21 (55.30-61.27)	58.03 (55.33-60.68)	58.12 (55.43-61.21)
6	50.17 (47.28-51.62)	50.01 (47.89-51.44)	50.15 (45.93-51.90)
7	56.20 (48.65-59.49)	56.17 (50.00-59.20)	56.11 (48.93-59.41)
8	58.10 (52.62-61.41)	57.93 (52.61-61.05)	58.09 (52.62-61.33)
9	34.12 (32.36-36.56)	34.14 (31.50-36.83)	34.16 (32.49-36.44)

The same trend was also seen in figure 8, where monitor units are compared for the three generated plans. Both the derived plans had less monitor units as compared to the original plan. The Plan_{UTESim} deviated less than two monitor units for all plans while the Plan_{MRISim} deviated more than five monitor units for all plans.

Table 9. The relative differences in mean, minimum and maximum dose to PTV (in separate rows) for the derived plans as compared to the original plan given in %

Patient number	Relative differences in mean, minimum and maximum dose to PTV [%]	
	Plan _{MRISim}	Plan _{UTESim}
1	-0.05	-0.30
	0.44	-0.08
	-0.13	-0.10
2	-0.29	-0.21
	0.00	-0.22
	-0.97	-0.40
3	0.23	-0.17
	-1.43	-0.30
	0.68	-0.06
4	-0.36	-0.08
	-0.31	0.44
	-1.06	-0.15
5	-0.31	-0.15
	0.05	0.24
	-0.96	-0.10
6	-0.32	-0.04
	1.29	-2.86
	-0.35	0.54
7	-0.05	-0.16
	2.77	0.58
	-0.49	-0.13
8	-0.29	-0.02
	-0.02	0.00
	-0.59	-0.13
9	0.06	0.12
	-2.66	0.40
	0.74	-0.33

The OAR with maximum deviation in maximum dose, expressed in percentage, for each plan comparing Plan_{UTESim} to the original plan were in all but one case less than 2 %, whereas only once under 2 % comparing Plan_{MRISim} to the original plan, as seen in table 10.

Table 10. The OAR with maximum deviation of maximum dose, expressed in %, for each plan when comparing the derived plans to the original plans.

Patient number	Plan	OAR with largest difference in max dose compared to original plan in percentage	Dose difference in percentage compared to original plan [%]	Dose difference [Gy]
1	Plan _{MRISim}	Left eye	-3.41	-0.07
	Plan _{UTESim}	Right eye	1.27	0.05
2	Plan _{MRISim}	Right lens	-5.68	-0.13
	Plan _{UTESim}	Left eye	-1.33	-0.03
3	Plan _{MRISim}	Left lens	-2.00	-0.01
	Plan _{UTESim}	Right lens	-1.49	-0.01
4	Plan _{MRISim}	Right eye	2.22	0.01
	Plan _{UTESim}	Right eye	-2.22	-0.01
5	Plan _{MRISim}	Right eye	-4.14	-0.13
	Plan _{UTESim}	Right lens	-0.59	-0.01
6	Plan _{MRISim}	Right eye	-5.14	-0.11
	Plan _{UTESim}	Right eye	-1.40	-0.03
7	Plan _{MRISim}	Cochlea	5.61	1.36
	Plan _{UTESim}	Pons	-1.78	-0.97
8	Plan _{MRISim}	Right eye	-0.77	-0.23
	Plan _{UTESim}	Optic chiasm	0.34	0.18
9	Plan _{MRISim}	Left eye	-2.35	-0.12
	Plan _{UTESim}	Right eye	-1.33	-0.03

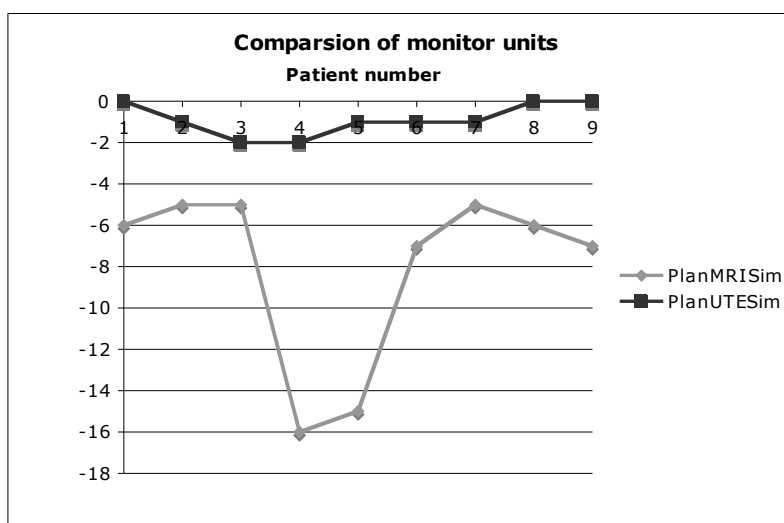


Figure 8. Difference in monitor units for the derived plans as compared to the original plan.

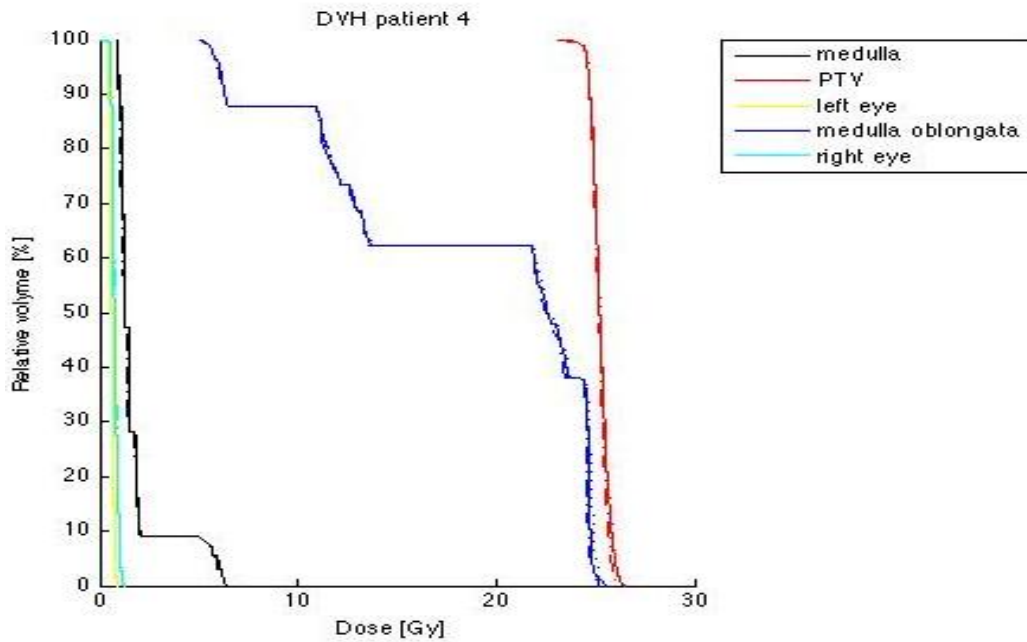


Figure 9. Typical DVH for the derived and the original treatment plans. The original plan is denoted by dots, $Plan_{MRISim}$ denoted by dashdots and $Plan_{UTESim}$ denoted by solid lines.

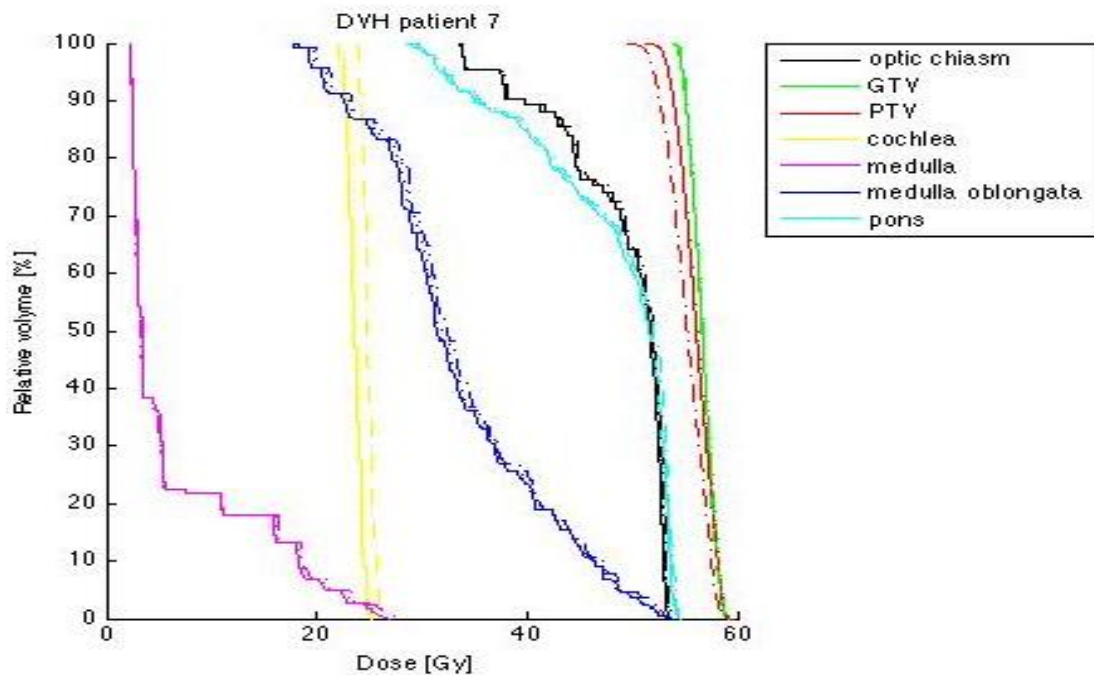


Figure 10. DVH with the greatest differences between the original and the derived plans for the 3D CRT. The original plan is denoted by dots, $Plan_{MRISim}$ denoted by dashdots and $Plan_{UTESim}$ denoted by solid lines

4.3.2 IMRT

Table 11-13 display differences between the derived plans as compared to the original plan when the same optimization was used. The plans were differing in final dose calculation. The mean dose to PTV for the three patients differed only slightly with an overall mean value of 1.35 ± 0.74 % and 0.02 ± 0.19 % for Plan_{MRISim} and Plan_{UTESim} as compared to the original, respectively. Corresponding mean values for the deviation in maximum and minimum dose to PTV were for Plan_{MRISim} 1.31 ± 0.84 % and 2.28 ± 64.12 , respectively and for Plan_{UTESim} 0.27 ± 0.65 % and 0.19 ± 0.59 , respectively. Comparing these plans in regard to the OAR with maximum deviation in maximum dose, expressed in percentage, for each plan comparing the derived plans to the original plan revealed that Plan_{UTESim} did not deviate more than 1.1 % for either of the patients with a mean value of 0.91 ± 0.11 % whereas the corresponding values for Plan_{MRISim} was 4.0 % with a mean value of 3.00 ± 0.76 %. The DVH for the plans generated for patient 11 and 12 overlapped for most structures but the largest differences were seen between the original plan and the Plan_{MRISim}. For patient number 10, which was a more complex case, slightly larger differences were seen.

Table 14-16 display differences between the plans where both the optimization and the final dose calculation is renewed for Plan_{UTESim} and Plan_{UTESim}. The mean dose to PTV for the three patients differ only slightly with an overall mean value of 0.02 ± 0.99 % and -0.07 ± 0.71 % for Plan_{MRISim} and Plan_{UTESim} as compared to the original, respectively. Mean values for the deviation in maximum and minimum dose to PTV are for Plan_{MRISim} -1.13 ± 2.16 % and 3.98 ± 61.57 , respectively and for Plan_{UTESim} 0.36 ± 2.70 % and -17.40 ± 22.47 , respectively. The deviation in maximum dose to OAR show a great variation ranging from 4.6 Gy to -6.0 Gy for Plan_{UTESim} and from 4.2 Gy to -5.9 Gy for Plan_{MRISim}. These differences are also seen in the DVH, figure 12.

Table 14. Mean, minimum and maximum dose to PTV, given in Gy, using the same optimization but different final dose calculations for the derived plans as compared to the original plan

Patient number	Mean dose (min – max) [Gy]		
	Original CT	Plan _{MRISim}	Plan _{UTESim}
10	46.21 (35.49-52.93)	47.34 (0-54.18)	46.24 (35.59-53.40)
	46.22 (19.06-52.56)	46.43 (20.25-52.82)	46.14 (18.95-52.42)
	46.01 (14.64-49.68)	46.29 (29.67-49.80)	45.90 (14.48-49.34)
11	54.38 (51.64-58.77)	55.16 (51.75-59.59)	54.49 (51.57-59.02)
12	55.20 (50.33-58.49)	56.19 (51.47-59.70)	55.33 (50.61-59.06)

Table 212. The relative differences in mean, minimum and maximum dose to PTV, given in %, using the same optimization but different final dose calculations for the derived plans as compared to the original plan

Patient number	Relative difference in mean, minimum and maximum dose to PTV [%]	
	Plan _{MRISim}	Plan _{UTESim}
10	0.45	-0.17
	6.24	-0.58
	0.50	-0.27
	0.61	-0.24
	102.66	-1.09
	0.24	-0.68
	2.45	-0.06
11	-100	0.28
	2.36	0.89
	1.43	0.20
12	0.21	-0.14
	1.40	0.43
	1.79	0.24
12	2.27	0.56
	2.07	0.97

Table 313. The OAR with maximum deviation of maximum dose, expressed in %, for each plan using the same optimization but different final dose calculations for the derived plans as compared to the original plans.

Patient number	Plan	OAR with largest difference in max dose compared to original plan in percentage	Dose difference in percentage compared to original plan [%]	Dose difference [Gy]
10	Plan _{MRISim}	Left cochlea	4.0	1.6
	Plan _{UTESim}	Brain	0.8	0.4
11	Plan _{MRISim}	Left cochlea	2.1	1.2
	Plan _{UTESim}	Right cochlea	1.1	0.4
12	Plan _{MRISim}	Left lens	2.9	0.4
	Plan _{UTESim}	Left cochlea	0.9	0.3

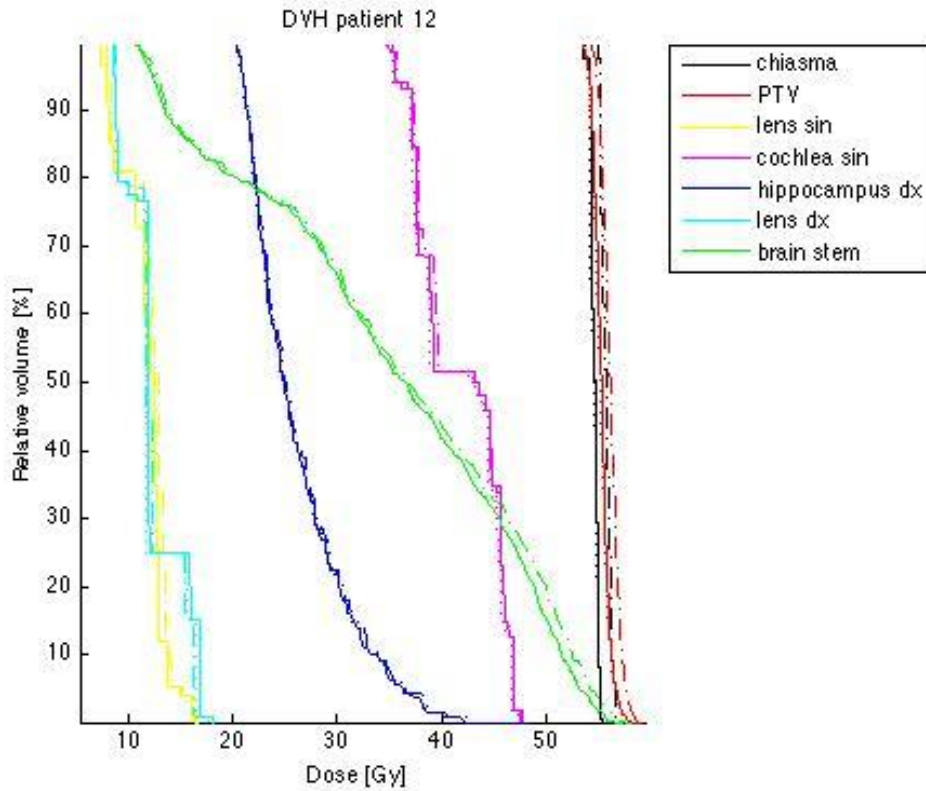


Figure 11. DVH for the derived and the original treatment plans differing only in final dose calculations. Original plan is denoted by dots, Plan_{MRISim} denoted by dashdots and Plan_{UTESim} denoted by solid lines.

Table 414. Mean, minimum and maximum dose to PTV, given in Gy, using different optimization and different final dose calculations for the derived plans as compared to the original

Patient number	Mean dose (min – max) [Gy]		
	Original CT	Plan _{MRISim}	Plan _{UTESim}
10	46.21 (35.49-52.93)	46.79 (0-51.80)	46.82 (35.96-55.06)
	46.22 (19.06-52.56)	45.86 (24.42-50.07)	46.13 (12.34-50.46)
	46.01 (14.64-49.68)	45.34 (27.93-50.24)	45.78 (6.90-50.10)
11	54.38 (51.64-58.77)	54.63 (52.55-58.27)	54.12 (51.64-57.63)
12	55.20 (50.33-58.49)	55.53 (49.95-59.03)	54.92 (50.19-58.05)

Table 515. The relative differences in mean, minimum and maximum dose to PTV, given in %, using different optimization and different final dose calculations for the derived plans as compared to the original

Patient number	Relative difference in mean, minimum and maximum dose to PTV [%]	
	Plan _{MRISim}	Plan _{UTESim}
10	-0.78	-0.19
	28.12	-35.26
	-4.74	-4.00
	-1.46	-0.50
	90.78	-52.87
	1.13	0.85
11	1.26	1.32
	-100	1.32
	-2.13	4.02
	0.46	-0.48
12	1.76	0
	-0.85	-1.94
	0.60	-0.51
12	-0.76	-0.28
	0.92	-0.75

Table 616. The OAR with maximum deviation of maximum dose, expressed in %, for each plan using different optimization and different final dose calculations for the derived plans as compared to the original plans.

Patient number	Plan	OAR with largest difference in max dose compared to original plan in percentage	Dose difference in percentage compared to original plan [%]	Dose difference [Gy]
10	Plan _{MRISim}	Right sowpod	15.0	0.8
	Plan _{UTESim}	Right sowpod	17.6	0.9
11	Plan _{MRISim}	Right opticus	6.3	3.1
	Plan _{UTESim}	Right bulb	7.8	2.5
12	Plan _{MRISim}	Right hippocampus	7.0	2.9
	Plan _{UTESim}	Right hippocampus	7.2	3.0

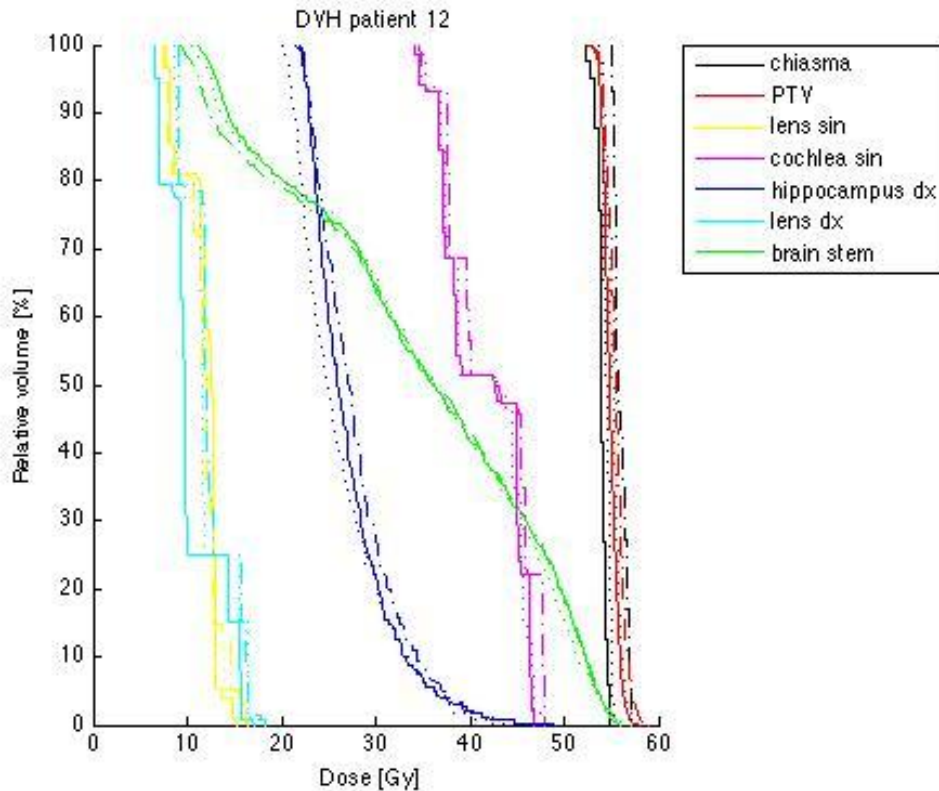


Figure 12. DVH for the derived and the original treatment plans differing both in optimization and final dose calculation. Original plan is denoted by dots, $Plan_{MRISim}$ denoted by dashdots and $Plan_{UTESim}$ denoted by solid lines.

5. Discussion

5.1 Distortion

The first step in the process of investigating radiotherapy treatment planning based solely on MRI-images should be to quantify the system induced geometric distortions. This is crucial since it influences the location of the organs and any pathologies within the image and hence could affect the delineation and the exact location of the target and OAR in the patient, which ultimately could lead to a poor treatment [2, 13]. The problem has been addressed by Doran *et al.* [13] who claimed that this should be a step in the quality assurance for clinics aiming to use MRI-based treatment plans for radiotherapy.

The ultimate evaluation of the system-induced distortions should be performed with a phantom enabling localization of markers in 3D to quantify the geometric distortions in 3D as well, as stated by Wang *et al.* [14]. This enables quantification of the distortions both within the 2D image as well as of the imaging plane, i.e. the slice selection direction. The phantom used in this work did not provide information regarding the distortion in the third dimension, since the phantom was made of PMMA rods going in one direction, hence quantification of the distortion was only performed in the imaging plane. The problem related to the third imaging dimension has partly been solved by imaging the phantom in three different rotations with respect to the MRI and CT scanner's long axis, (axial-, sagittal- and coronal direction), retrieving information of the system-induced distortions from all the gradients in the MRI scanner. However, true 3D evaluation can only be performed

using a 3D phantom. The difficulty in positioning the phantom accurately on the curved tabletop of the MRI scanner, in order to allow imaging in the three directions, was tedious and associated with a positional uncertainty. This uncertainty was expected to be no less than 1 mm and affecting the overall result when matching the positions in the MR-images with that of the CT-template. The four outmost positions (see numbers in figure 2) in all slices are plotted in figures 3-4, 13-14 and 16-18 for each pulse sequence in order to evaluate the system-induced distortions in the imaging plane. These positions were thought to be most prone to system-induced distortions since they are furthest from the isocenter of the magnet bore and associated with the highest values of the magnetic field gradients used for image resolution [1]. To somewhat investigate the system-induced distortions in the slice encoding direction, the outmost positions of the phantom are plotted for all slices (figures 5, 15, 18) for all pulse sequence. If there existed severe distortions in the slice selection direction these would possibly be seen in these figures. In these graphs, any mispositioning of the phantom can also be retrieved.

The uncertainties arising from matching MR-images against a CT-template was considered to be a lesser problem than the probably larger discrepancies that would appear if all the actual slices from the two imaging sessions, with slightly different positionings, would have been compared. The method to compare the center of gravity of the dots in the images for all slices acquired by MRI to those values of center of gravity in the CT-template is associated with uncertainties since these values have to be rounded off to be expressed as a single pixel value. Perhaps having rods with a smaller diameter could reduce this uncertainty although it would also have the effect of reducing the differences in signal between the rods and the surrounding water. The spatial resolution also affects the center of gravity of the positions and sets the ultimate level of the accuracy for which the distortion can be quantified. A higher spatial image resolution allows a better approximation of the center of gravity of the position of the rods in the images. Thresholding the signal intensity in the images contribute to the uncertainty of only considering the center of gravity for the positions as well. The MR-image signal intensity was largely affected by the positioning of the receiving coils. In some images the slices in the middle showed less intensity than those at the end although a 3D-homogeneity correction was applied to all images. In other slices, image signal intensity dropped at the end of the phantom reducing the number of slices that could be compared against the CT-template. For the UTE-images in the sagittal- and coronal slice direction simple thresholding of the signal intensity was impossible since the intensity varied quite largely within the imaging volume. Instead of thresholding the signal intensity, an edge detection filter was applied before retrieving the center of gravity of each PMMA rod in the images for comparison against that of the CT-template. The largest deviation of 6.8 mm found in the sagittal UTE-images is misleading since it was a result of air close to a rod, which with the edge detection filter, was misinterpreted as one area. By omitting these regions in the two affected slices the absolute maximum deviation compared to the CT-template was reduced to 2 mm and the absolute maximum deviation in the x- and y direction was both 2.7 mm. The large deviation in the T1W images, acquired in the axial direction, was explained by the fact that the phantom appeared rotated due to a poor selection of the slice positioning before image acquisition. The slight deviations in the T1W sequence (figure 3-5) as compared to the T2W sequence (Appendix) are within the uncertainties considering the positioning and the method of finding the center of gravity of the positions and should not be interpreted as a larger distortion in the T1W sequence.

The absolute maximum differences, displayed in table 4-6, are the maximum distortions for a single position within the phantom. This position was often found in one of the slices close to the edge of the phantom and probably, it could be better explained by a slight tilt of the phantom rather than caused by geometric distortions. The majority of the pixels has much smaller deviations, as shown by the absolute mean values of the differences in positions for all pulse sequences and imaged with the phantom in the three different directions. For the T1W images with the vendor's distortion correction, only 0.4 % of the pixels show an absolute maximum distortion greater than 2 mm when omitting the T1W measurement where the phantom was rotated. Corresponding values both for the T2W and the UTE pulse sequence with the vendor's distortion correction are 0.3 % and 0.1 %, respectively. These results show less system-induced distortion in the imaging volume (3 dm³) than what was found by Doran *et al.* [14] but they used an imaging volume 9 times as large, almost 29 dm³. Comparing the measurements with and without the vendor's distortion correction reveals that the correction routine reduces the distortions with 13-50 %. This is less than the observation by Wang *et al.* [11]. Their study found system-induced distortions in the imaging plane within a volume 3.6 dm³, which is slightly larger than the volume examined with our stereotactic phantom.

One alternative to avoid using a CT-template, and reduce the positional uncertainties when using two modalities, would be to know the physical position of each reference position within the phantom. Wang *et al.* [14] does not describe how they obtain this information but it is assumed that they know the actual positions beforehand. An uncertainty with that method is that PMMA can alter its shape with time and temperature and hence, the positions can be altered [5]. Another alternative is described by Doran *et al.* [13], who states that a set of spherical harmonics can be used to approximate the magnetic field caused by the gradients of the MRI-scanner and through this method obtain information about the undistorted positions. The disadvantages with this approach is that it requires information from the vendors, since it is what they use for correction of the distortion caused by the gradients, it assumes that this information is correct and it only applies to distortions caused by the gradients.

5.2 The UTE pulse sequence

In the UTE-images of the four volunteers, a variation of the signal intensity was observed (figure 6). These intensity variations depend, in most cases on the position of the flex coil, showing high signal intensity close to the coil and less intensity remote from the coil.

Other areas that displayed high signal intensity in the short UTE-echo for all volunteers were the orbita and the area close to the temporal muscle as seen in Figure 6. The signal from bone was seen to vary some in the short UTE-echo. Images from this short echo show a lack of tissue contrast but producing the subtraction map greatly enhanced the contrast from bone as well as the skin surrounding the head. In the subtraction maps the variations of signal intensities within the bone are enhanced, especially in the bone forming the skull. This is caused by signal within the bone that remain in the second echo. The subtraction hence produces an additional inhomogeneity to these areas containing bone. Otherwise the generated subtraction maps cancelled signal from tissues with longer T₂, such as the brain, effectively. For all volunteers, high signal intensity areas were seen in the periphery of the head in the short UTE-echo and these were even more apparent in the subtraction map. The short

UTE-echo is less affected by susceptibility effects and the protons have less time to become out of phase for shorter TEs compared to the second echo, which is more prone to susceptibility effects. Producing the subtraction maps hence introduces possible susceptibility artefacts and perhaps this could be part of the explanation to the signal enhancement seen in the periphery of the head. Although the images produced with the UTE pulse sequence show a lack of contrast and are quite blurry, they can still be of great value in radiotherapy treatment planning since they can distinguish areas corresponding to bone from areas corresponding to air. With conventional MRI pulse sequences these areas are both attributed by low signal intensity that often cannot be separated.

The 3D dual echo UTE pulse sequence used in this study collects the signal in a spherical k-space trajectory, a kooshball. This renders an extra difficulty when choosing the volume to be imaged since it is difficult to place the FOV for the kooshball to enable a full collection of images data of the head. This was made apparent in figure 6 where the nose was “cut off” in the images for two of the four volunteers. The solution would be to extend the FOV but since the signal is collected isotropically this results in a prolonged scan time. An alternative would be to collect k-space differently by the use of Shifting TE Phase –encoded Stack of Stars trajectory (STEPS) [17]. This differs from the kooshball in that it uses a phase encoding gradient for slice selection [17]. The advantages with STEPS include the opportunity of having thicker slices than the in plane resolution enabling a reduction of the scan time as compared to kooshball [17]. Both STEPS and the kooshball UTE pulse sequences are for clinical research and has yet to be approved before used in the clinic.

5.3 Segmentation

A simply thresholding of high signal intensity pixels in the short UTE-echo or in the subtraction map was not adequate for segmentation of bone areas. Instead, information from the short UTE-echo was used to differentiate bone from air, areas which in the second echo are categorized by low intensity. Choosing the threshold of the signal intensity when segmenting bone was conducted by guidance both by anatomy books concerning the head and by the CT-images of the patients from the treatment planning study. Comparing the mean volume of bone segmented from all four volunteers with a mean volume of the areas considered as bone when segmenting the CT-images in OMP (before assigning bulk densities) is very similar. The value derived from the UTE-images was $530 \pm 157 \text{ cm}^3$ and $555 \pm 84 \text{ cm}^3$ was derived from the CT-images. The latter value is a mean value for 5 patients chosen based on the number of slices to correspond to the scanned volume with the MRI scanner. The standard deviation of the volume as determined with the UTE-based segmentation was much larger and the method had problems segmenting areas where the bone is very thin. The segmentation of these areas was hence underestimated whereas areas close to the temporal muscle were overestimated due high signal intensity in the subtraction map from this area.

The problems related to the area of the periphery of the head was to a large extent solved using the edge detection filter but a few pixels, commonly positioned close to the nose and ear, were still misinterpreted as bone. The problem could be further reduced, altering the widening of the outer area received from the edge detection filter for each volunteer. However, this was not done since the method for segmentation was to be standardized. The only parameter varied between the volunteers was the

intensity value used for thresholding in the short UTE-echo, in the longer echo and in the subtraction map. These values were only varied slightly. It should be emphasized that the UTE pulse sequence used in this work has not been optimized for segmentation since this work only was aimed at evaluating if segmentation of bone was possible. Optimization of the pulse sequence would probably improve the segmentation. To fully evaluate the performance of the segmentation, scanning of the same patient with both modalities is necessary. Scanning a patient could also give information of the potential influence of the tumour on the segmentation. Diseases may alter the T2 relaxation time of a certain tissue due to a change of concentration of T2-components [15]. It has been reported that metastases from malignant melanoma appear as high signal intensity in images acquired with the UTE pulse sequences [15]. For tumours and edema, an increase of T2 relaxation and hence a reduction of short T2 components, are common and this would lead to low intensity pixels in the subtraction map as well as in the UTE-echo [15]. Scanning a patient with both modalities will also provide an opportunity to evaluate if the segmentation of the UTE-images could be used as DRR. If the UTE-images can be used as DRR, MRI take a step closer of becoming an alternative to CT-based treatment planning, at least for tumours to the head.

5.4 Treatment planning

5.4.1 3D CRT

As seen in the results the deviations in mean, minimum and maximum dose to PTV as well as maximum dose to OAR were less for Plan_{UTESim} compared to the deviations for Plan_{MRISim}, when these plans are compared against the original plan. This was also confirmed when considering the difference in monitor units when comparing the derived plans to the original plan. For the majority of the patients the mean, minimum and maximum doses to target were slightly underestimated for both the segmented plans and the water approximated plans as compared to the original plan. An underestimation of the dose is a result from an overestimation of the attenuation of the beam. This is the case when the beam passes through large air cavities for the plan calculated based on approximating the head to a volume of water. For Plan_{UTESim} this can occur if the segmentation underestimates the amount of air or overestimates the attenuation of the bone. The evaluation of the isodoses for each plan is made difficult since OMP cannot save dose calculations for the same patient when the structures are altered even though they are saved as different plans. This made a direct comparison between the original plans and Plan_{UTESim} impossible. Instead the comparison of the isodoses had to be against Plan_{MRISim} for both the original plan as well as for Plan_{UTESim}. In general Plan_{MRISim} gave a seemingly better and more homogenous coverage of target as compared to the original plan. Differences in isodoses were greatest in CT-slices where the beams penetrate air cavities or through bone where Plan_{MRISim} shifts the isodoses for target towards lower doses or towards higher doses, respectively. This is of course due to an over approximation of the attenuation in air and an under approximation of the attenuation in bone as compared to water. Plan_{MRISim} also displayed less hotspots as compared to the original plan. Plan_{UTESim} show close resemblance to the original plan except for a few slices that include large contents of bone where target coverage was less than the original plan. However, the comparison with Plan_{UTESim} against the original is very uncertain due to reasons described above.

The maximum differences in maximum dose to OAR in percentage comparing the original plan with Plan_{UTESim} and with Plan_{MRISim} are shown in table 9. Except for patient number 7, the differences were very small when displayed in Gy, where the greatest difference being 0.36 Gy seen in Plan_{MRISim}. The deviation was greatest to the cochlea in Plan_{MRISim} and to the pons for Plan_{UTESim}. For this patient the target was situated very close to air cavities, hence the beams penetrate through air. The overestimation of the dose to cochlea is a result from this air penetration and the overestimation of the attenuation. Similarly the underestimation to pons achieved with Plan_{UTESim} is probably due to an overestimation of the areas being segmented as bone and/or an underestimation of the areas segmented as air in regions surrounding the target. This slight uncertainty in segmentation is also the reason why patient number 7 displayed the largest differences comparing the DVH for all plans, seen in figure 10. Overall the DVH of OARs and the target volumes were very similar for the three generated plans for each patient. Plan_{MRISim} tended to overestimate the dose to the OAR if only slightly.

Except for patient number 2 no maximum doses to critical organs are exceeded. For this patient the dose to the brain stem exceeds 54 Gy in all created plans even in the original plan indicating that this plan was mistaken as the approved one when exporting the different cases to the OMP student system where all additional treatment plans for 3D CRT were constructed. This was still included in the study since, even if it was not a clinical approved plan it can still be used in the comparison of treatment plans.

5.4.2 IMRT

Comparing the results for the derived plans, differing only in final dose calculation, with the original plans, the same trend as for the 3D CRT could be seen. The Plan_{UTESim} was more similar to the original plan in regard to mean, minimum and maximum dose to PTV, dose to OAR, DVH and isodoses though the latter cannot be accurately compared. Comparing isodoses are, for all the IMRT patients, difficult since they demonstrate a more complex pattern as compared to the 3D CRT patients. The difference in dose to PTV was larger comparing Plan_{MRISim} and Plan_{UTESim} to the original plan than for the 3D CRT plans, indicating that segmentation of tissue is better suited for IMRT. This was especially seen in patient number 10 where the minimum and maximum dose to PTV showed great deviations comparing Plan_{MRISim} to the original plan. Plan_{UTESim} displayed a very close resemblance to the original plan in dose to OAR as well as for the DVH stressing this further. The values achieved in this study are comparable to those obtained by Stanescu *et al.* of less than 1 % difference in mean, max and minimum dose to PTV for the plans generated with bulk densities [6 ,7]. These authors segmented brain, scalp and bone and not as in this study soft tissue, bone and air. They used a five beams arrangement but none of the papers describe if any of the beams penetrate through large air cavities. Omitting the heterogeneity corrections gave a difference of 2-3 % comparing the DVH obtained with the original plans. This is a slightly greater deviation than the values gained comparing the original plan with Plan_{MRISim}.

To perform a new optimization on a different image base will of course give altered fluences resulting in large differences, as is the case for the derived plans; Plan_{MRISim} and Plan_{UTESim} as compared to the original plan (table 13-15, figure 12). If IMRT was to be done solely based on MR-images a new optimization would of course have to be performed so these plans can give an idea of the uncertainties associated by doing

IMRT solely based on MR-images. The doses to OAR differed greatly even expressed in Gy and similar values for maximum dose to OAR as given in table 15 could also be seen in the mean doses for the OAR. These differences in dose are surprisingly large for Plan_{UTESim} and are not clinically acceptable. The greatest differences were seen for small organs such as the lenses, which only included a small number of voxels and hence can be associated with larger uncertainties. One possible reason for these discrepancies could be that the segmentation, especially the region in the vicinity of the nose where differentiating bone from soft tissue is difficult, will result in incorrectly classified areas leading to deviations in dose. The beams for the IMRT patients all penetrate through large air cavities unlike the plans for the 3D CRT. In the latter the patient with beams penetrating through air displayed the greatest differences as compared to the original plan. With more beams penetrating through air and including areas where the segmentation is uncertain will produce a greater variation in dose, as seen in the IMRT plans. The differences are largest for patient number 10. This patient had a tumor in the nose and two additional targets in the neck region. This was a complex case and the positions of the targets were situated in areas with large inhomogeneities. The differences in minimum and maximum dose to PTV were huge for the derived plans when compared to the original. For the other two patients with targets located in the head the differences in maximum and minimum dose to PTV were comparable to those seen when using the same optimization. However, the maximum dose to OAR still showed great deviations for all the patients, as stated above. A further analyze of the reason for the large differences in dose for these IMRT plans could be to create IMRT plans for all the 3D CRT patients used in this study. These plans could be analyzed pixel by pixel to achieve a distribution over the differences, which could give further information about the deviation.

5.5 Future work

Since this is the first project within this area at Lund University Hospital, many steps remain before MR-images can be used alone for external radiotherapy treatment planning. The next obvious step for a full evaluation of treatment planning as well as the performance of the segmentation based on the UTE-images is to scan a patient with both modalities, as has already been stated above. Stanescu *et al.* found a larger difference when doing treatment planning on their MR-images [6, 7] and this could then be further investigated. Treatment planning on the segmented UTE-images would also render an evaluation of the possible misclassification in the segmentation and its affect on the dose calculations possible. Another obvious step is to make the treatment planning system accept MR-images for planning. Today images from MRI are fused to those obtained with CT. Comparing bony landmarks in images of the same patient taken with CT and the UTE pulse sequence can also give information of the use of these MR-images as DRR. As for the UTE pulse sequence, further studies of cancelling tissue with preparation pulses to gain improved contrast in the short UTE-echo as well as scanning using STEPS is another area of research that would be of interest. This would perhaps also improve the segmentation. An investigation of the performance of the UTE pulse sequence with the flex coils in the pelvis area and/or with large FOV would also be of interest.

Many articles written within the subject of treatment planning using MR-images alone have focused on prostate cancer. This is perhaps the area where MRI could be of most importance since the prostate and neighbouring OAR are hard to visualize with CT-images. The next step within this subject would therefore be to build a larger phantom that should have dimensions large enough to cover a FOV used for imaging the pelvis

of patients. This phantom should be made such that evaluation of the system-induced distortions in 3D is made possible, which would also probably reduce the uncertainties concerning positioning of the phantom since imaging of the phantom in different directions could be omitted. . Before using only MRI-images for treatment planning in external radiotherapy it would also be of interest to investigate object induced distortions.

6. Conclusion

Considering the uncertainties due to the difficulties in positioning the phantom in the MRI scanner due to its curved table top and the inaccuracies in the method of comparing the center of gravity for the positions found in the MRI-images against the center of gravity for the positions found in the CT-template, the results showed that the distortions were mostly less than the 2 mm demand required for radiotherapy and no correction is needed. This is however, only true when applying the vendor's distortion correction and within the investigated volume, otherwise the system-induced distortions may be larger. The differences obtained when comparing the center of gravity for the positions in the phantom from images acquired by the two modalities are similar for all pulse sequences tested.

Imaging with the UTE pulse sequence enabled detection of bone signal within the head of all four volunteers. Producing the subtraction map greatly enhanced the image contrast, which in the shortest echo was relatively isointense. Information from the subtraction maps and the short UTE-echo made the segmentation of bone and air feasible. The periphery of the head was at first categorized as bone but using an edge detection filter on the second echo and subtracting the obtained area from those already considered as bone, solved this problem to a large extent.

For conformal radiotherapy, dose calculations based on approximating the head to one homogenous volume gave clinically acceptable deviations as compared to the CT-based plan considering dose to target. Segmentation of the MR-images into bone, soft tissue and air is therefore not mandatory but give a very close resemblance to the dose distribution calculated from the CT-images considering dose to different OAR as well as dose to PTV. Similar deviations to those achieved with 3D CRT were obtained for the IMRT plans generated using the same optimization. The dosimetric differences with $\text{Plan}_{\text{UTESim}}$ showed a closer resemblance to the original plan than those achieved with $\text{Plan}_{\text{MRISim}}$ when considering mean, minimum and maximum dose to PTV, dose to OAR and the DVHs. This is indicating that segmentation of tissue is better suited for IMRT. However, making an optimization followed by a dose calculation based on the derived plans gave large deviations to OAR as well as in minimum and maximum dose to PTV. Such optimization would have to be done if IMRT intended to be based entirely on MR-images; hence further studies are needed to deduce the reasons for these deviations.

Adding the UTE pulse sequence to the imaging protocol, normally including T1W- and the T2W-pulse sequences, when imaging patients obviously results in a prolonged scan time (an increase of about 10 min) but has the advantage of making a more accurate treatment planning possible. This could lead to MRI being used even in more complicated cases, but more patients are needed for evaluation before this can be completely ensured, as indicated in this study. However, the UTE pulse sequence holds great promise in external radiotherapy. For the aim to be completely fulfilled scanning a patient with both imaging modalities is necessary which, would give full

information of the performance of the segmentation method and enable a dosimetric evaluation of the MRI-images to be conducted as well.

Acknowledgements

I would like to give a big thank to my supervisors Sara Brockstedt for all her time (even with very short notice), support and opinions, Crister Ceberg for answering sudden questions and Tommy Knöös for letting me sit in the sauna. A special thank should also be given to Karin Markenroth-Bloch and Jimmy Lätt at the MR-department for all the help and answers concerning the UTE pulse sequence and when scanning the phantom.

References

1. Khoo V S, Joon D L., *New developments in MRI for target volume delineation in radiotherapy*. Br J Radiol, 2006; **79**: 2-15
2. Evans, P.M., *Anatomical imaging for radiotherapy*. Phys Med Biol, 2008; **53**(12):151-191
3. Chen L, Price Jr R.A, Wang L, Li J.S, Qin L, McNeeey S, Ma C-M, Freedman G, Pollack A., *Dosimetric evaluation of MRI-based treatment planning for prostate cancer*. Phys Med Biol, 2004; **49**(22): 5157-5170
4. Metcalf P, K.T., Hoban P., *The Physics of Radiotherapy X-ray and Electrons*. 2007, ISBN 978-1-930524-36-1, Medical Physics Publishing.
5. Tanner S F, Finnigan D J, Khoo V S, Mayles P, Dearnaley D P, Leach M O., *Radiotherapy treatment planning of the pelvis using distortion corrected MR images: the removal of system distortions*. Phys Med Biol, 2000; **45**: 2117-2132
6. Stanescu T, Jans H-S, Pervez N, Stavrev P, Fallone B G., *A study on the magnetic resonance imaging (MRI)-based radiation treatment planning of intracranial lesions*. Phys Med Biol, 2008. **53**(13): 3579-3593
7. Stanescu, T, Hans-Sonke J, Stavrev P, Fallone B G., *3T MR-based treatment planning for radiotherapy of brain lesions*. Radiol Oncol, 2006; **40**(2): 125-132
8. Fransson A, Andreo P, Pötter R., *Aspects of MR Image Distortions in Radiotherapy Treatment Planning*. Strahlenther Onkol., 2001 Feb; **177**(2): 59-73
9. Jonsson J., *Radiotherapy treatment planning based solely on magnetic resonance imaging: thesis paper for Master Science in Medical Radiation Physics*. 2008
10. Holmes J, Bydder G, *MR imaging with ultrashort TE (UTE) pulse sequence: Basic principles*. Radiography, 2005; **11**(3): 163-174
11. Wang D, Strugnell W, Cowin G, Doddrell D.M, Slaughter R, *Geometric distortion in clinical MRI systems Part I: evaluation using a 3D phantom*. Magn Reson Imaging, 2004; **22**(9): 1211-1221
12. Wang D, Strugnell W, Cowin G, Doddrell D.M, Slaughter R., *Geometric distortion in clinical MRI systems Part II: correction using a 3D phantom*. Magn Reson Imaging, 2004; **22**(9): 1223-1232
13. Doran S, Charles-Edwards L, Reinsberg S, Leach M., *A complete distortion correction for MR images: I. Gradient warp correction*. Phys Med Biol, 2005; **50**(7):1343-1361
14. Wang D, Doddrell D.M, Cowin G., *A novel phantom and method for comprehensive 3-dimensional measurement and correction of geometric distortion in magnetic resonance imaging*. Magn Reson Imaging, 2004; **22**(4): 529-542
15. Tyler D, Robson M, Henkelman M, Young I, Bydder G., *Magnetic resonance imaging with ultrashort TE (UTE) PULSE sequences: technical considerations*. J Magn Reson Imaging, 2007; **25**(2): 279-289
16. Robson, M.D, Bydder G.M., *Clinical ultrashort echo time imaging of bone and other connective tissues*. NMR Biomed, 2006, **19**(7): 765-780
17. Bos C, R.J., Schröder C, *Ultrashort Echo-Time Imaging: Instructions for Use*. 2008

18. ICRU, *Report 46 Photon, Electron, Proton and Neutron Interaction Data for Body Tissues*, ISBN 0-913394-41-6, 1992
19. Oncentra ® Masterplan Ver. 3.1, *Physics and Algorithms*, 4.6.4 Dose Statistics Calculations, 2008

7. Appendix

Distortion

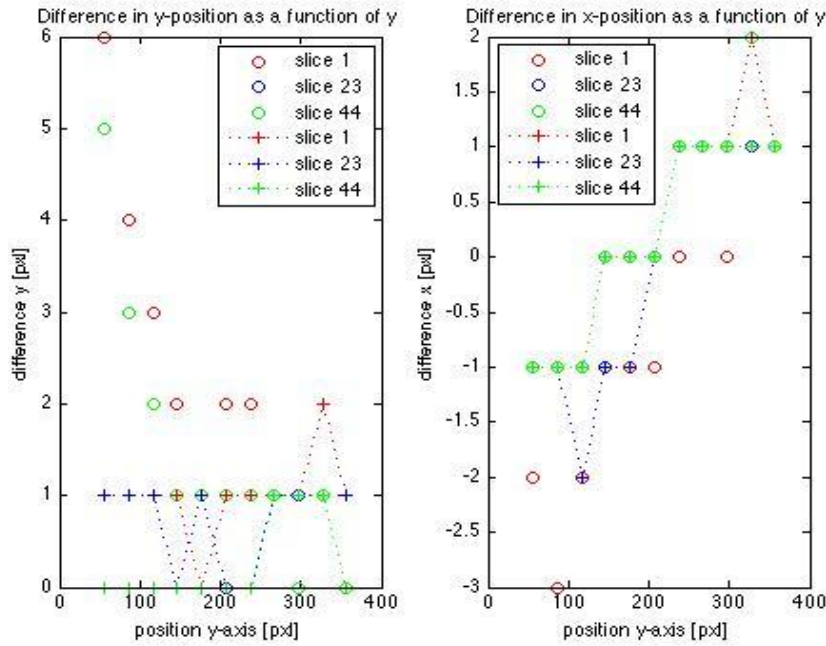


Figure 13. Difference in the coordinates in the anterior-posterior direction for the T2W pulse sequence. Measurement with the vendor's distortion correction applied is denoted with crosses whereas measurement without any distortion correction applied is denoted with circles.

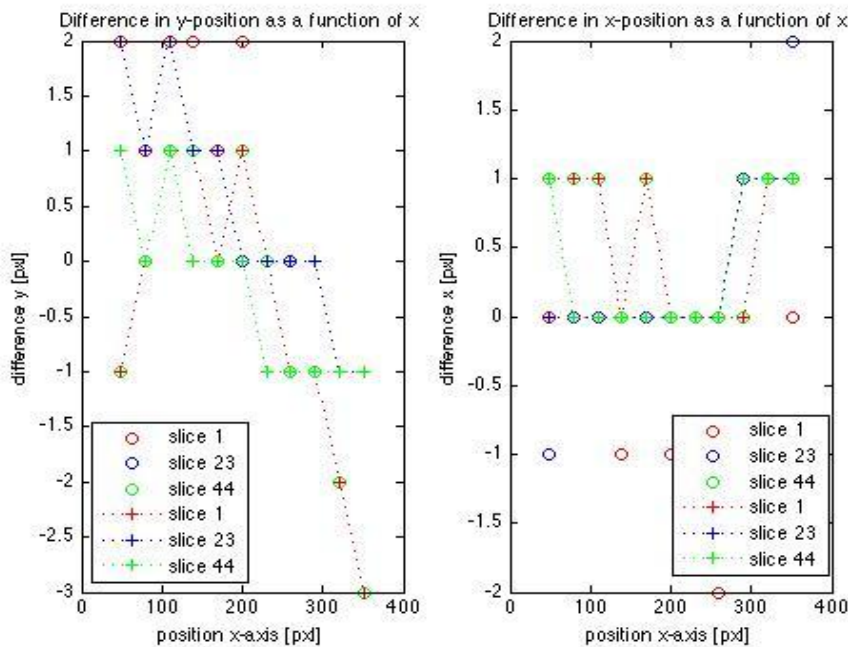


Figure 14. Difference in the coordinates in the dextral-sinistral direction for the T2W pulse sequence. Measurement with the vendor's distortion correction applied is denoted with crosses whereas measurement without any distortion correction applied is denoted with circles.

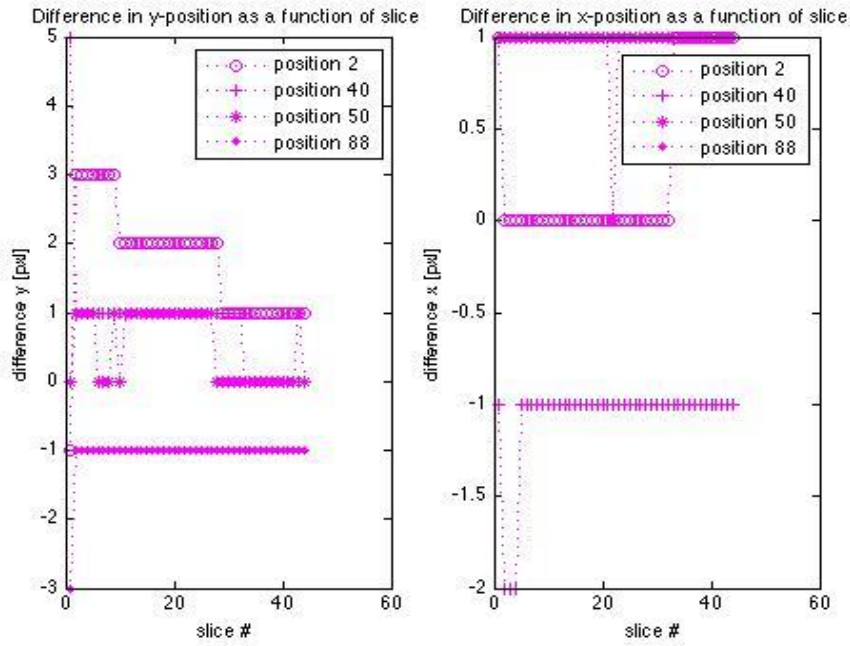


Figure 15. Difference in the coordinates in the cranial-caudal direction for the T2W pulse sequence. Only measurement with the vendor's distortion correction applied is shown.

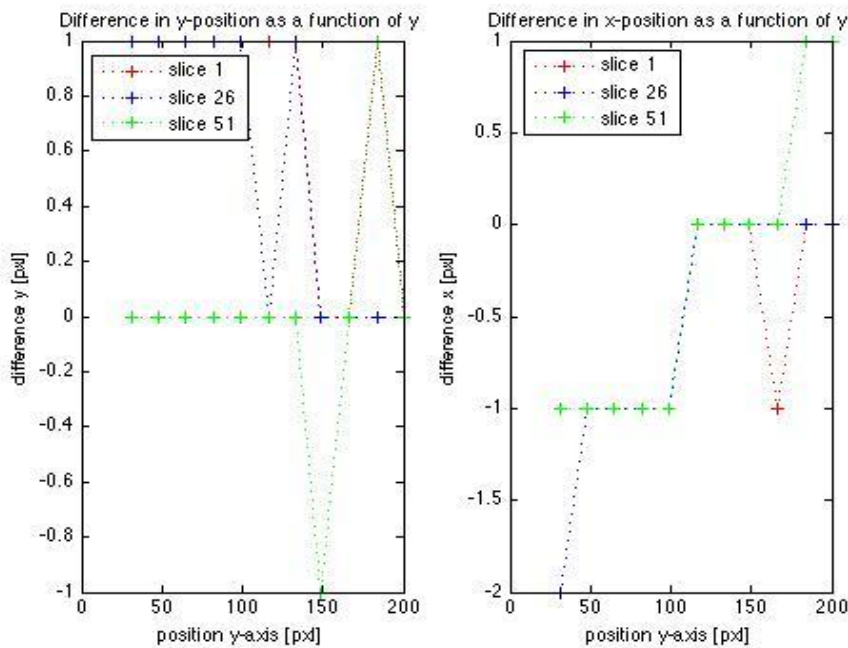


Figure 16. Difference in the coordinates in the anterior-posterior direction for the UTE pulse sequence. Only measurement with the vendor's distortion correction was conducted.

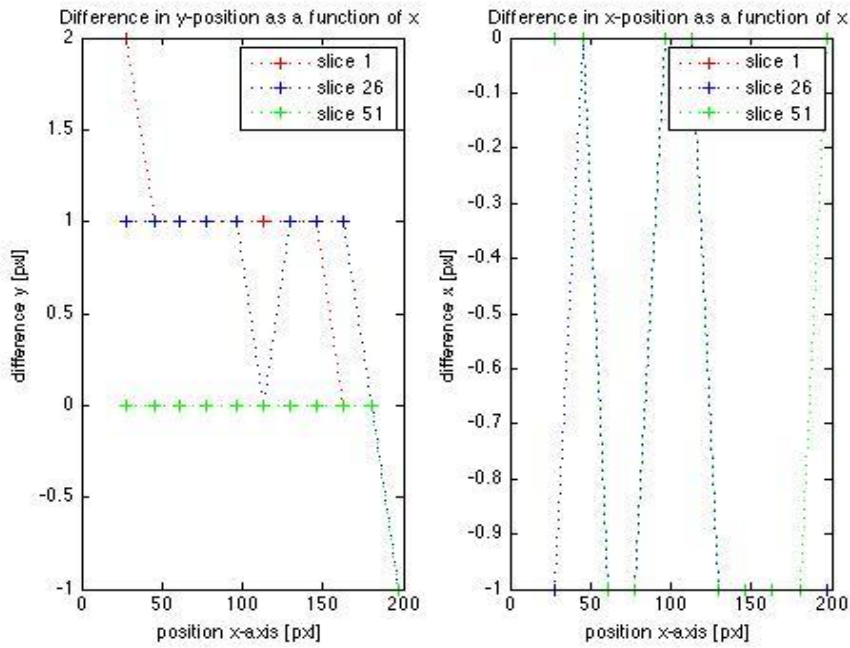


Figure 17. Difference in the coordinates in the dextral-sinistral direction for the UTE pulse sequence. Only measurement with the vendor's distortion correction was conducted.

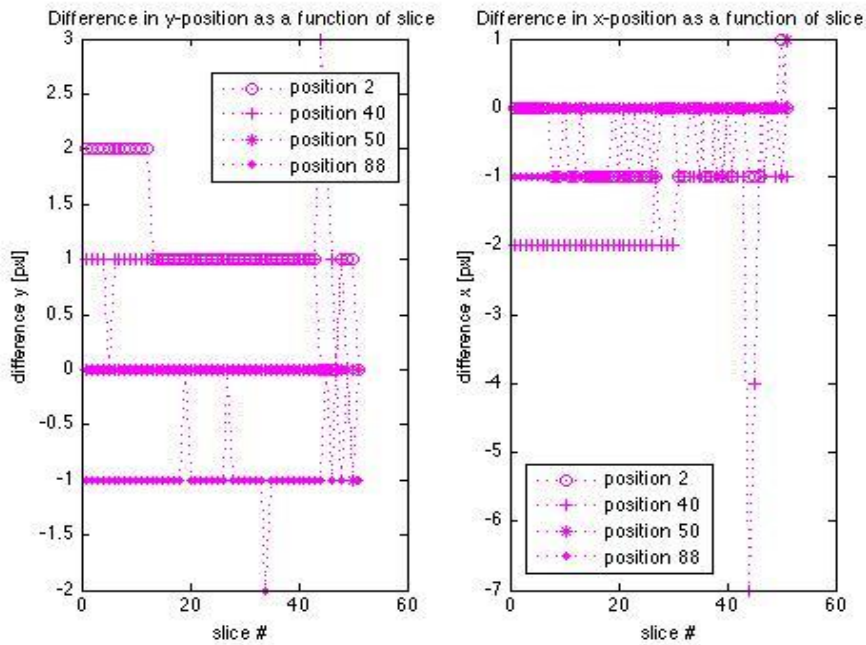


Figure 18. Difference in the coordinates as a function of slice in the cranial-caudal direction for the UTE pulse sequence. Only measurement with the vendor's distortion correction was conducted.